Supplementary Information

Matrix viscoelasticity controls spatio-temporal tissue organization

Alberto Elosegui-Artola, Anupam Gupta, Alexander J. Najibi, Bo Ri Seo, Ryan Garry, Christina M. Tringides, Irene de Lázaro, Max Darnell, Wei Gu, Qiao Zhou, David A. Weitz, L. Mahadevan, David J. Mooney

Supplementary information included in this file:

- Supplementary Note 1.
- Supplementary Figures 1 to 23.
- Supplementary text describing the model.
- Supplementary Tables 1 to 3.

Supplementary Note 1: Model dimensionless parameters

Systems with low μ correspond to relatively viscous matrices, while those with high μ correspond to matrices that are relatively fluid. When the scaled cell flux j is small, the pressure due to the growing tissue is not large enough to create fingers in the matrix, while when j is large, fingering likely arises as cells actively intrude into the matrix. Finally, systems with low values of A correspond to matrices that mechanically relax very slowly, while systems with high values of A correspond to matrices that relax very quickly. In our experiments and simulations, the ratio $\mu = \mu_t/\mu_m$ ∈[0.001-2], τ_a ∈[7-54]s, while τ_m ∈[1-350]s, so that the ratio A=τ_a/τ_m ∈[0.1-100], and finally with spheroid sizes R∼100 μm , and proliferative tissue timescale τ_t ∼[4-500] s, the ratio $j = \tau_\mathrm{g}/\tau_t$ ∈[0.002-0.25].

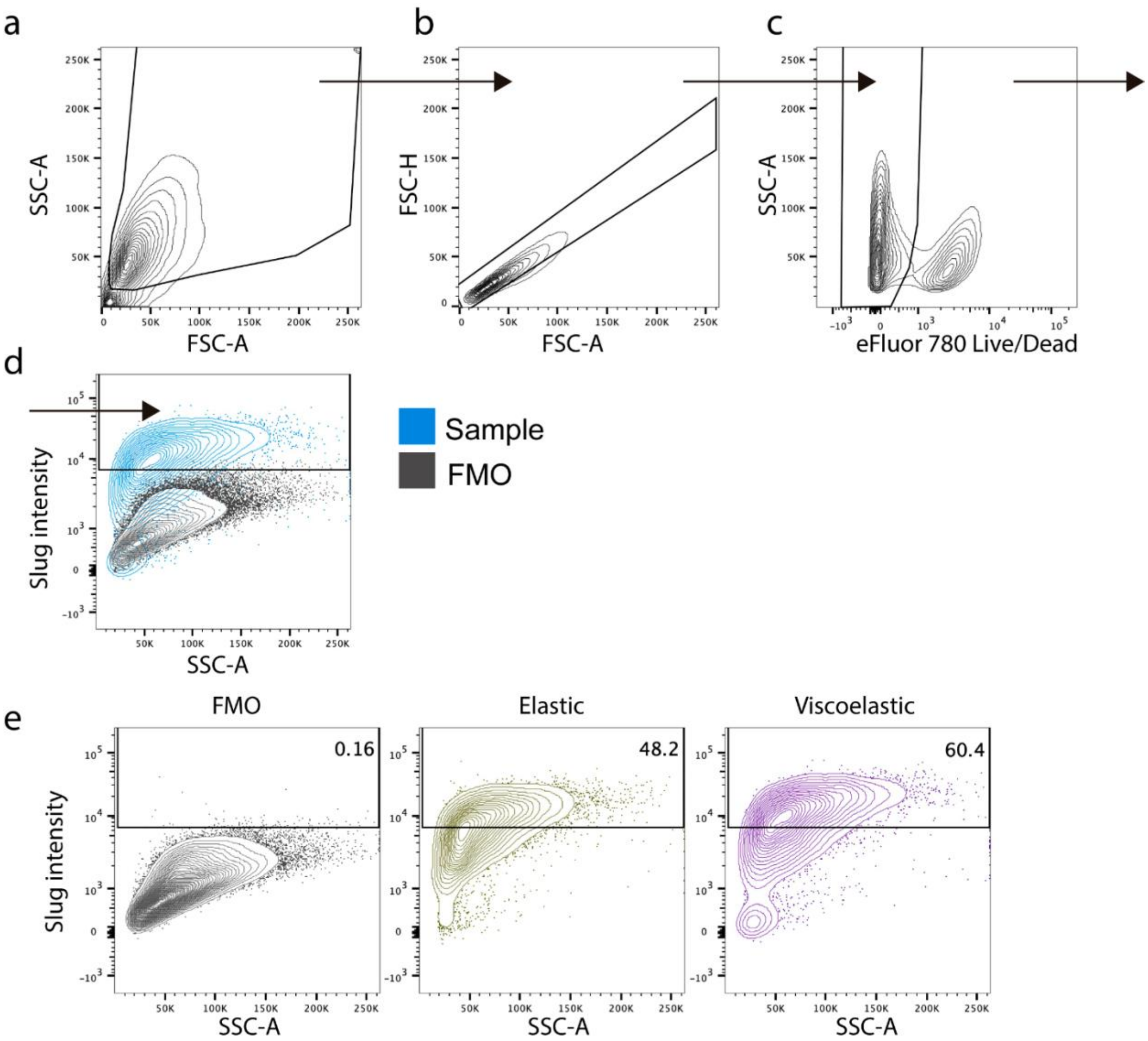

Supplementary Figure 1. Representative example of flow cytometry experiments. a-e, Representative gating strategy for Slug-expressing cells collected from alginate gels. Samples were gated for single (**a-b**), live cells (c) and Slug-expressing cells were identified using a fluorescence minus one (FMO) control (**d**). **e-g**, spheroids were cultured in elastic or viscoelastic alginate gels for 5 days and collected following gel digestion. Expression of EMT regulators was assessed through intracellular flow cytometry. **f**, Representative flow cytometry plots are shown for Slug expression.

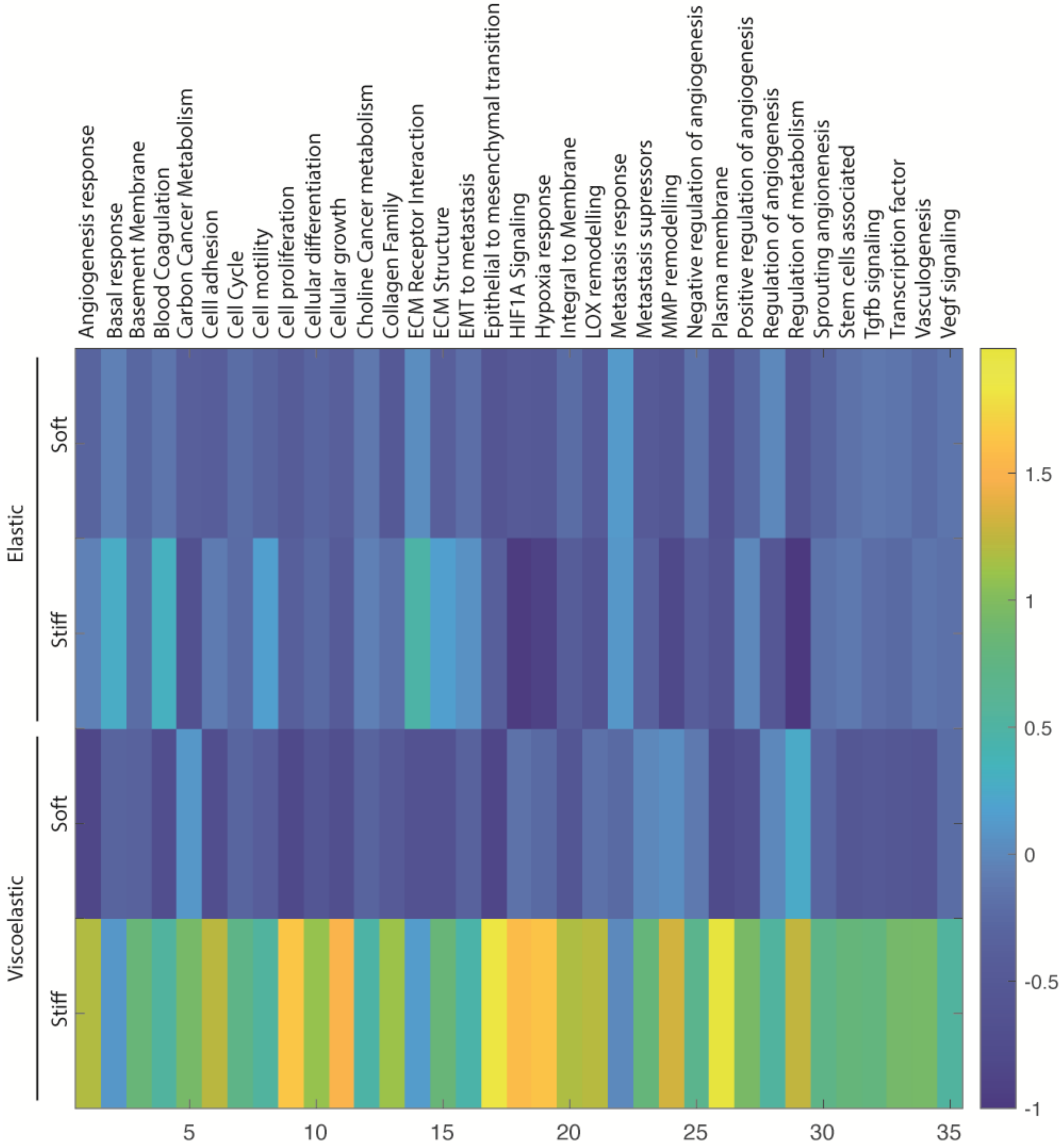

Supplementary Figure 2. Cancer pathway is upregulated in stiff viscoelastic matrices. Results of the regulation of cancer-related pathways after the analysis of the expression levels of 770 genes included in the Nanostring PanCancer Progression panel for spheroids in the matrices described.

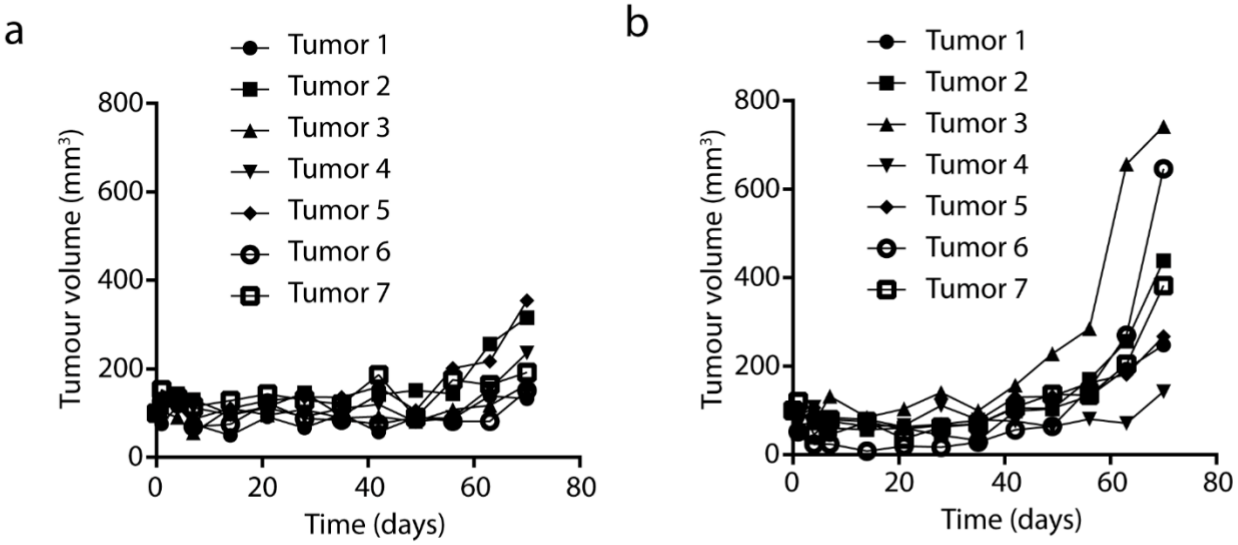

Supplementary Figure 3. Viscoelasticity increases tumor growth in mice. a-b, Quantification of MDA-MB-231 tumor volume evolution in NOD/SCID mice. MDA-MB-231 cells encapsulated in elastic (**a**) and viscoelastic (**b**) alginate gels were injected subcutaneously into mouse flanks and tumor growth was tracked externally using calipers. Each curve represents an independent tumor/mouse.

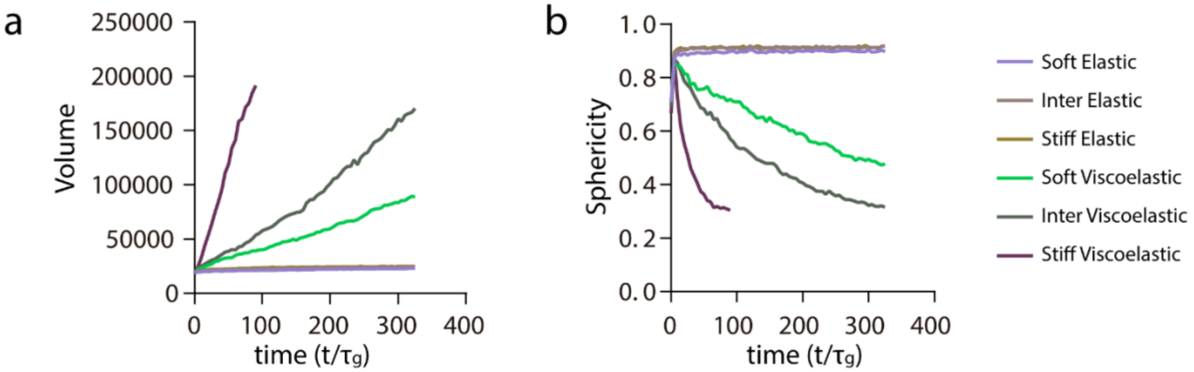

Supplementary Figure 4. Model predicts cell volume increase and sphericity decrease with stiffness in viscoelastic matrices. a-b, Quantification from the simulations of the volume (**a**) and sphericity (**b**) of the spheroids, respectively, over time for soft, intermediate and stiff elastic and viscoelastic matrices. The dimensionless parameter in the model for stiff elastic $\left(A = \frac{\tau_a}{\tau_m} = 0.4, \mu = \frac{\mu_t}{\mu_m} = 0.002, j = \frac{\tau_g}{\tau_t} = 0.05\right)$; intermediate elastic $\left(A = \frac{\tau_a}{\tau_m} = 0.13, \mu = \frac{\mu_t}{\mu_m} = 0.002, j = \frac{\tau_g}{\tau_t} = 0.05\right)$; soft elastic $\left(A = \frac{\tau_a}{\tau_m} = 0.003, \mu = \frac{\mu_t}{\mu_m} = 0.002, j = \frac{\tau_g}{\tau_t} = 0.04\right)$; stiff viscoelastic $\left(A = \frac{\tau_a}{\tau_m} = 400, \mu = \frac{\mu_t}{\mu_m} = 2, j = \frac{\tau_g}{\tau_t} = 0.22\right)$; intermediate viscoelastic $\left(A = \frac{\tau_a}{\tau_m} = 133, \mu = \frac{\mu_t}{\mu_m} = 2, j = \frac{\tau_g}{\tau_t} = 0.16\right)$; and soft viscoelastic $\left(A = \frac{\tau_a}{\tau_m} = 3.3, \mu = \frac{\mu_t}{\mu_m} = 2, j = \frac{\tau_g}{\tau_t} = 0.14\right)$ matrices.

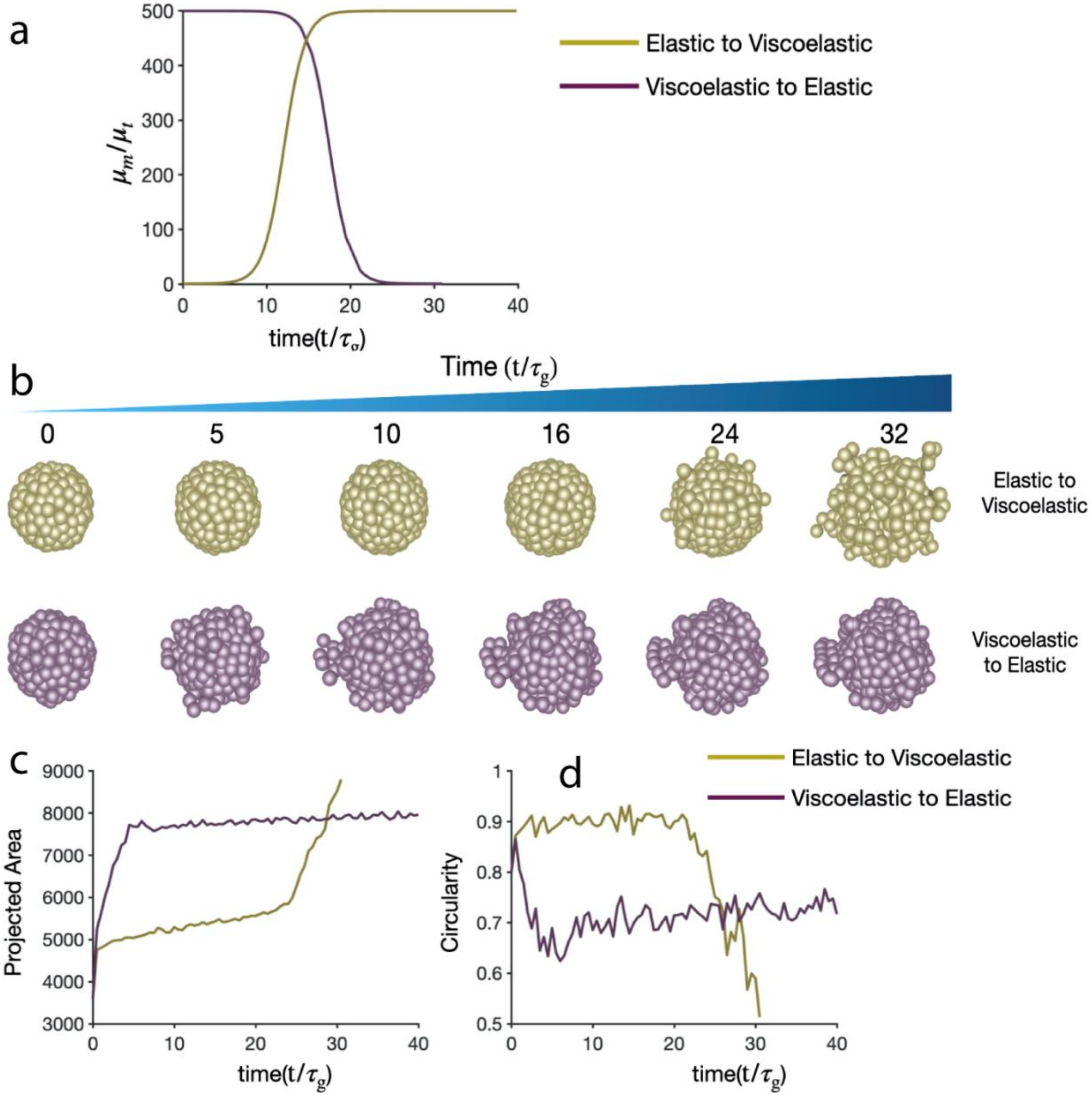

Supplementary Figure 5. Increasing/Decreasing the viscosity dynamically prevents/facilitates morphological instability a, Showing the change in the substrate to tissue viscosity ratio as a function of time, tissue viscosity has been kept fixed; Two cases have been considered, in the first case the matrix is changing its viscosity from high (elastic) to low (viscoelastic) and in the second case matrix changing its viscosity from low (viscoelastic) to high (elastic) **b,** Images of spheroids from the simulation where the viscosity of the matrix is changing dynamically over time from elastic to viscoelastic (top row) and from viscoelastic to elastic (bottom row) **c-d**, Simulation prediction of projected area (**c**) and circularity (**d**) evolution over time of spheroids while the viscosity of the matrix is changing dynamically. The corresponding dimensionless parameter in the model for the intermediate stiff matrix in the elastic and viscoelastic limit are $\left(A = \frac{\tau_\mathrm{a}}{\tau_\mathrm{m}} = 0.017, \mu = \frac{\mu_\mathrm{t}}{\mu_\mathrm{m}} = 0.002, j = \frac{\tau_\mathrm{g}}{\tau_\mathrm{t}} = 0.05\right)$ and $\left(A = \frac{\tau_\mathrm{a}}{\tau_\mathrm{m}} = 133, \mu = \frac{\mu_\mathrm{t}}{\mu_\mathrm{m}} = 2, j = \frac{\tau_\mathrm{g}}{\tau_\mathrm{t}} = 0.16\right)$, respectively.

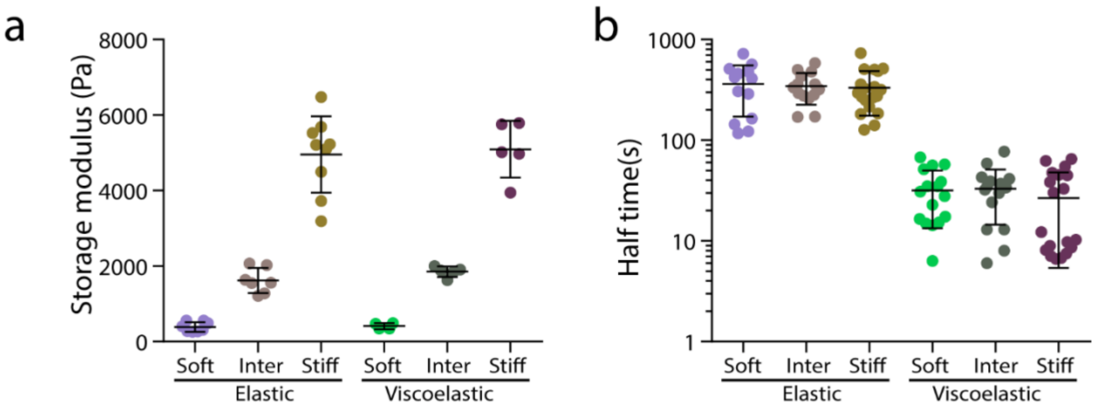

Supplementary Figure 6. Quantification of hydrogel mechanical properties. a, Quantification of the storage modulus of alginate hydrogels. n=8,4,5,7,9,5 gels per condition. **c,** Quantification of the timescale at which an initially applied stress is relaxed to half its original value. n=13,14,19,16,16,19 gels per condition. Error bars are s.d.

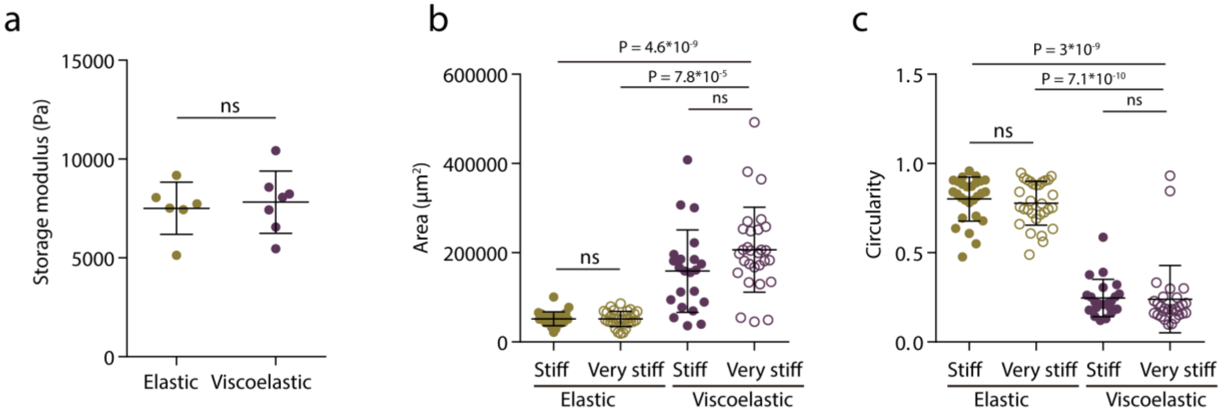

Supplementary Figure 7. Quantification of spheroids response to stiffer hydrogels. a, Quantification of the storage moduli of alginate hydrogels**.** n=6,7 gels per condition. Statistical analysis was performed using Mann-Whitney U-test. **b-c**, quantification of spheroids area (**b**) and circularity (**c**) in different stiffness inelastic and viscoelastic hydrogels. n= 27,30,22,29 spheroids per condition. Statistical analysis was performed using Kruskal–Wallis test followed by post hoc Dunn's test. All data represent mean ± s.d.

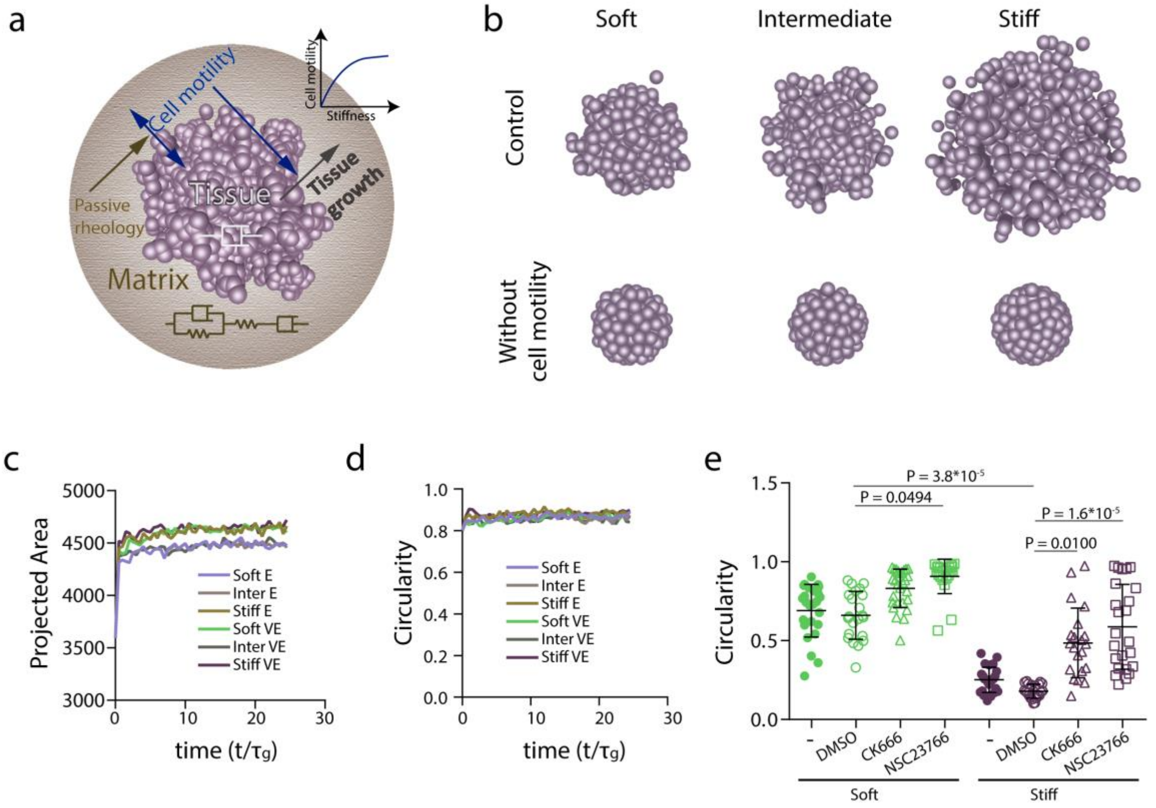

Supplementary Figure 8. Inhibition of cell motility prevents morphological instability, independent of gel stiffness. a, The influence of eliminating cell motility, in gels with varying stiffness, was simulated in the model. **b,** Images of spheroids, from final timepoint of simulation, in increasingly stiff viscoelastic gels in control case (upper row) and when cell motility was suppressed (lower row). **c-d,** Simulation prediction of projected area (**c**) and circularity (**d**) evolution over time of spheroids in increasingly stiff viscoelastic and elastic gels when cell motility was suppressed (lower row). The dimensionless parameter in the model for stiff elastic $\left(A = \frac{\tau_\mathrm{a}}{\tau_\mathrm{m}} = 0.03, \mu = \frac{\mu_\mathrm{t}}{\mu_\mathrm{m}} = 0.002, j = \frac{\tau_\mathrm{g}}{\tau_\mathrm{t}} \sim 0\right)$; intermediate elastic $\left(A = \frac{\tau_\mathrm{a}}{\tau_\mathrm{m}} = 0.017, \mu = \frac{\mu_\mathrm{t}}{\mu_\mathrm{m}} = 0.002, j = \frac{\tau_\mathrm{g}}{\tau_\mathrm{t}} \sim 0\right)$; soft elastic $\left(A = \frac{\tau_\mathrm{a}}{\tau_\mathrm{m}} = 0.0017, \mu = \frac{\mu_\mathrm{t}}{\mu_\mathrm{m}} = 0.002, j = \frac{\tau_\mathrm{g}}{\tau_\mathrm{t}} \sim 0\right)$; stiff viscoelastic $\left(A = \frac{\tau_\mathrm{a}}{\tau_\mathrm{m}} = 33.3, \mu = \frac{\mu_\mathrm{t}}{\mu_\mathrm{m}} = 2, j = \frac{\tau_\mathrm{g}}{\tau_\mathrm{t}} \sim 0\right)$; intermediate viscoelastic $\left(A = \frac{\tau_\mathrm{a}}{\tau_\mathrm{m}} = 16.7, \mu = \frac{\mu_\mathrm{t}}{\mu_\mathrm{m}} = 2, j = \frac{\tau_\mathrm{g}}{\tau_\mathrm{t}} \sim 0\right)$; and soft viscoelastic $\left(A = \frac{\tau_\mathrm{a}}{\tau_\mathrm{m}} = 1.7, \mu = \frac{\mu_\mathrm{t}}{\mu_\mathrm{m}} = 2, j = \frac{\tau_\mathrm{g}}{\tau_\mathrm{t}} \sim 0\right)$ matrices. **e,** Quantification of spheroids circularity after 5 days in soft and stiff viscoelastic matrices with Arp2/3 (CK666) and Rac1 (NSC23766) inhibitors. n=24,21,21,24,25,22,27,21 spheroids per condition. Statistical analysis was performed using Kruskal–Wallis test followed by post hoc Dunn's test. All data represent mean ± s.d.

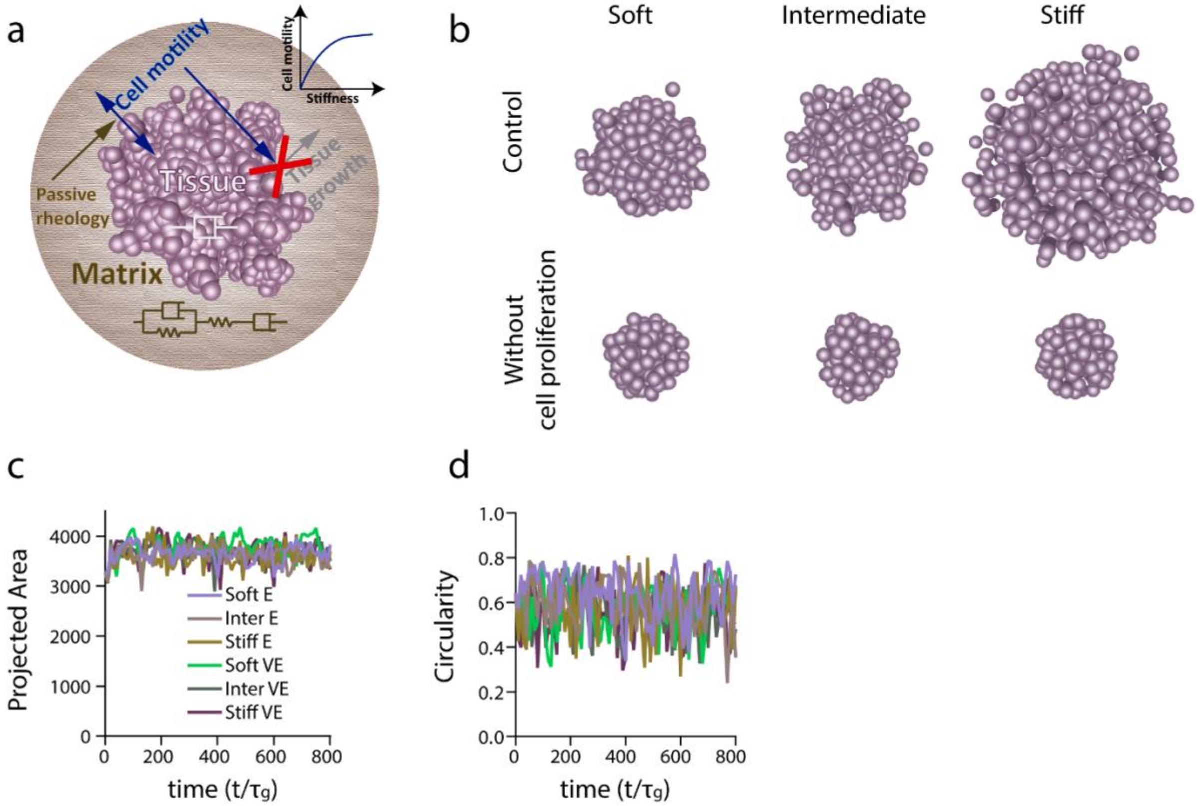

Supplementary Figure 9. Inhibition of cell proliferation prevents morphological instability independently of the gel stiffness. a, the influence of eliminating cell proliferation, in gels of increasing stiffness, was simulated in the model. **b,** Images of spheroids, from final timepoint of simulation, in increasingly stiff viscoelastic gels in control case (upper row) and when cell proliferation was inhibited. **c-d**, Simulation prediction of projected area (**c**) and circularity (**d**) evolution over time of spheroids in increasingly stiff elastic and viscoelastic gels when cell proliferation was suppressed. The dimensionless parameter in the model for stiff elastic $\left(A = \frac{\tau_\mathrm{a}}{\tau_\mathrm{m}} = 0.4, \mu = \frac{\mu_\mathrm{t}}{\mu_\mathrm{m}} = 0.002, j = \frac{\tau_\mathrm{g}}{\tau_\mathrm{t}} = 0\right)$; inter elastic $\left(A = \frac{\tau_\mathrm{a}}{\tau_\mathrm{m}} = 0.13, \mu = \frac{\mu_\mathrm{t}}{\mu_\mathrm{m}} = 0.002, j = \frac{\tau_\mathrm{g}}{\tau_\mathrm{t}} = 0\right)$; soft elastic $\left(A = \frac{\tau_\mathrm{a}}{\tau_\mathrm{m}} = 0.003, \mu = \frac{\mu_\mathrm{t}}{\mu_\mathrm{m}} = 0.002, j = \frac{\tau_\mathrm{g}}{\tau_\mathrm{t}} = 0\right)$; stiff viscoelastic $\left(A = \frac{\tau_\mathrm{a}}{\tau_\mathrm{m}} = 400, \mu = \frac{\mu_\mathrm{t}}{\mu_\mathrm{m}} = 2, j = \frac{\tau_\mathrm{g}}{\tau_\mathrm{t}} = 0\right)$; inter viscoelastic $\left(A = \frac{\tau_\mathrm{a}}{\tau_\mathrm{m}} = 133.3, \mu = \frac{\mu_\mathrm{t}}{\mu_\mathrm{m}} = 2, j = \frac{\tau_\mathrm{g}}{\tau_\mathrm{t}} = 0\right)$; and soft viscoelastic $\left(A = \frac{\tau_\mathrm{a}}{\tau_\mathrm{m}} = 3.33, \mu = \frac{\mu_\mathrm{t}}{\mu_\mathrm{m}} = 2, j = \frac{\tau_\mathrm{g}}{\tau_\mathrm{t}} = 0\right)$ matrices.

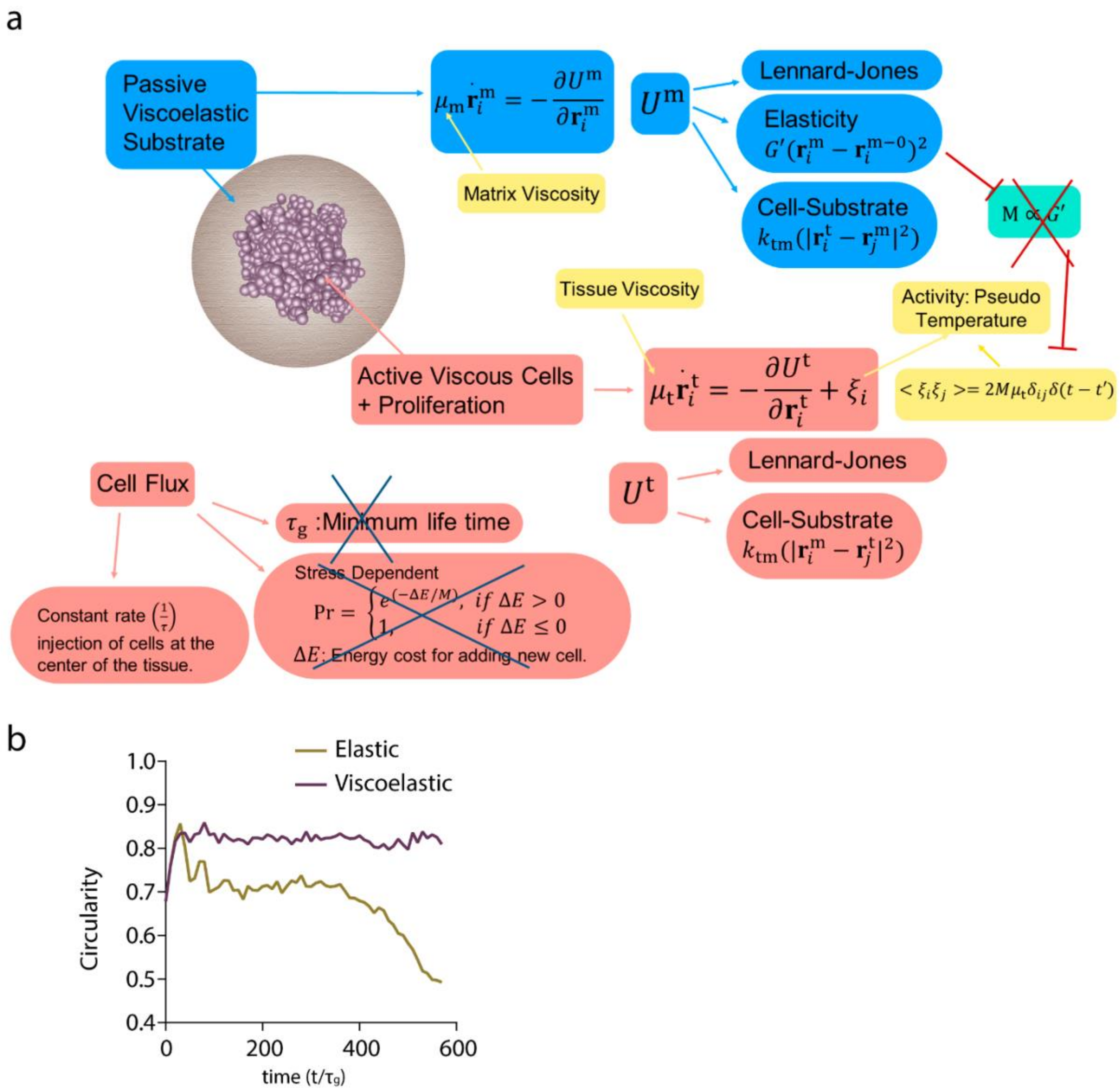

Supplementary Figure 10. a, 3D model for cell flux driven simulations. The texts in light blue/light red color boxes describe the matrix/cell property and interactions therein. The yellow boxes represent the parameters which we vary to probe the phase space of morphologies. The cells are being injected at the center of the tissue to mimic the experiments and hence the proliferation is independent of the stress. Now motility is not a function of stiffness and its value has been chosen to be very small. **b**, Quantification from the simulations of the circularity of the spheroids.

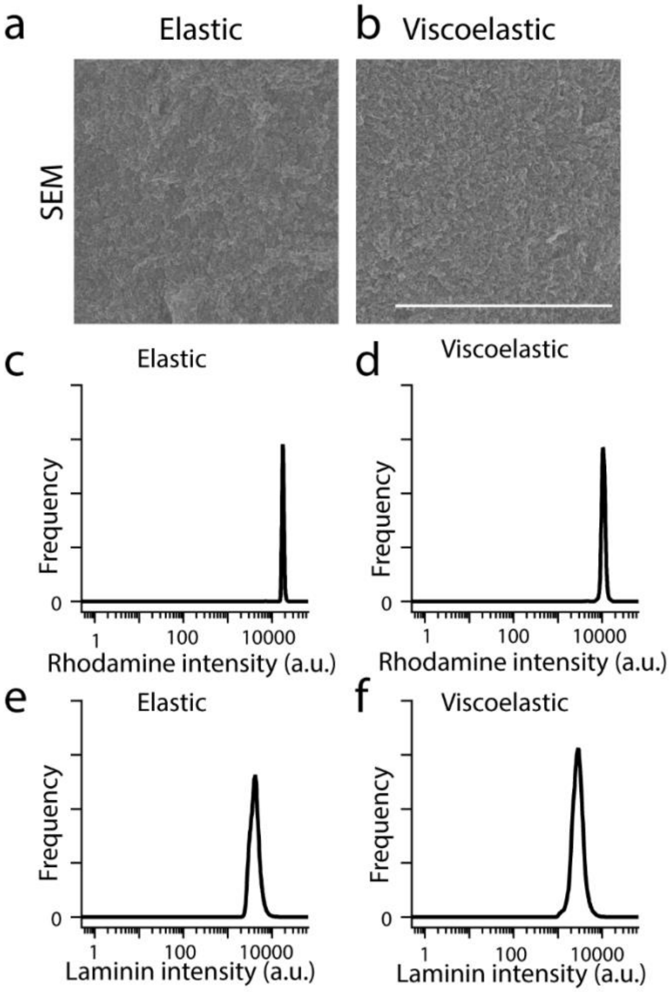

Supplementary Figure 11. Alginate-matrigel interpenetrating networks are homogeneous without micro-scale phase separation. a-b, Representative scanning electron micrographs, of an alginate-matrigel matrix for the (a) elastic and the (b) viscoelastic condition. There is no phase separation. n> 30 images per condition. **c-d**, Representative histograms of fluorescent alginate of an (c) elastic and (d) viscoelastic interpenetrating matrix. **e-f**, Representative histograms of laminin staining of an (e) elastic and (f) viscoelastic interpenetrating matrix. The presence of alginate and laminin staining in each pixel demonstrates that these two networks are interpenetrating at this scale. Scale bar is 10 µm.

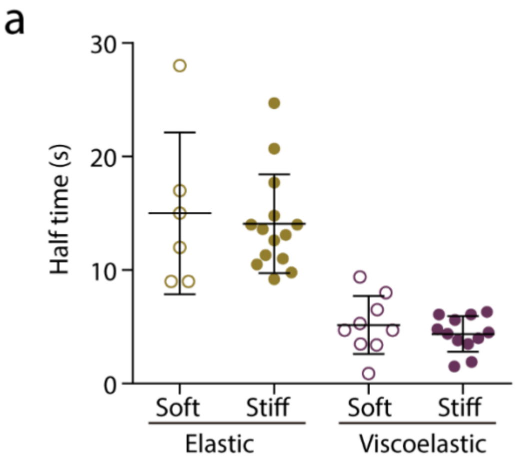

Supplementary Figure 12. Stresses relax faster in interpenetrating networks polymerized with lower molecular weight alginate. **a**, Half time of alginate-matrigel interpenetrating networks. n=6,14,9,12 gels per condition. Data represent mean ± s.d.

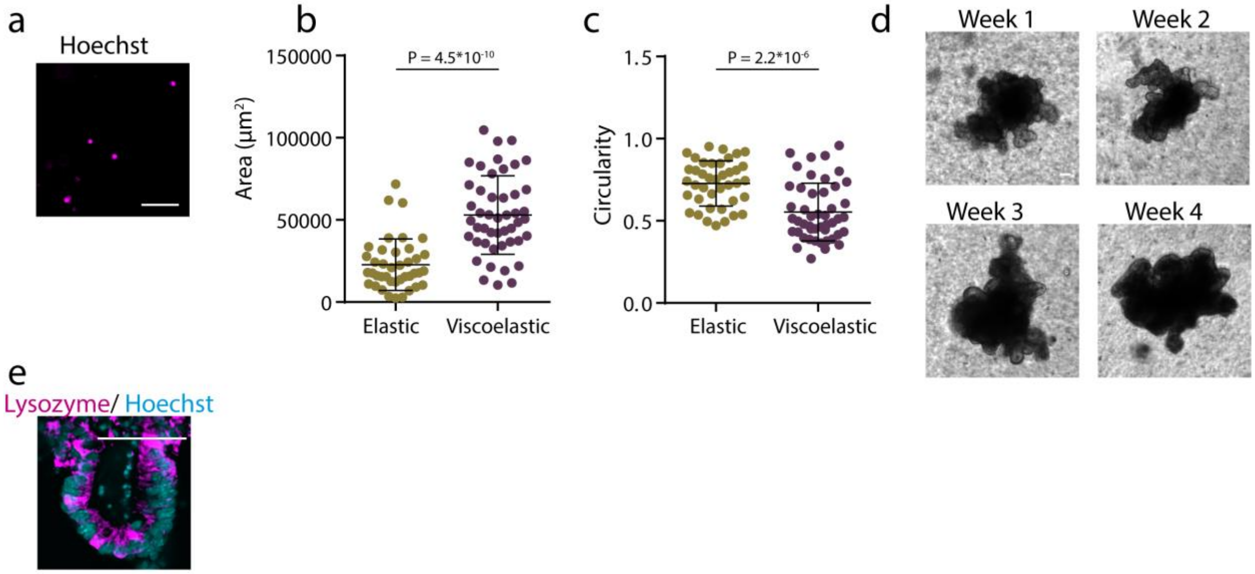

Supplementary Figure 13. Single cells form organoids in interpenetrating alginate and Matrigel networks. a, Single cells were encapsulated in interpenetrating networks. n= 11 images. **b-c**, Quantification of organoids area (c) and circularity (d) after 7 days in elastic and viscoelastic interpenetrating networks. b-c, n=40,47 organoids per condition. Statistical analysis was performed using two-sided Mann-Whitney U-test. **d**, Organoids were passed, broken down to single cells and encapsulated in new interpenetrating networks every 7 days. n > 25 images per condition. **e**, After one month of passaging, Paneth cells were visualized by lysozyme staining. n = 6 images. Data represent mean ± s.d. Scale bars are 50 µm.

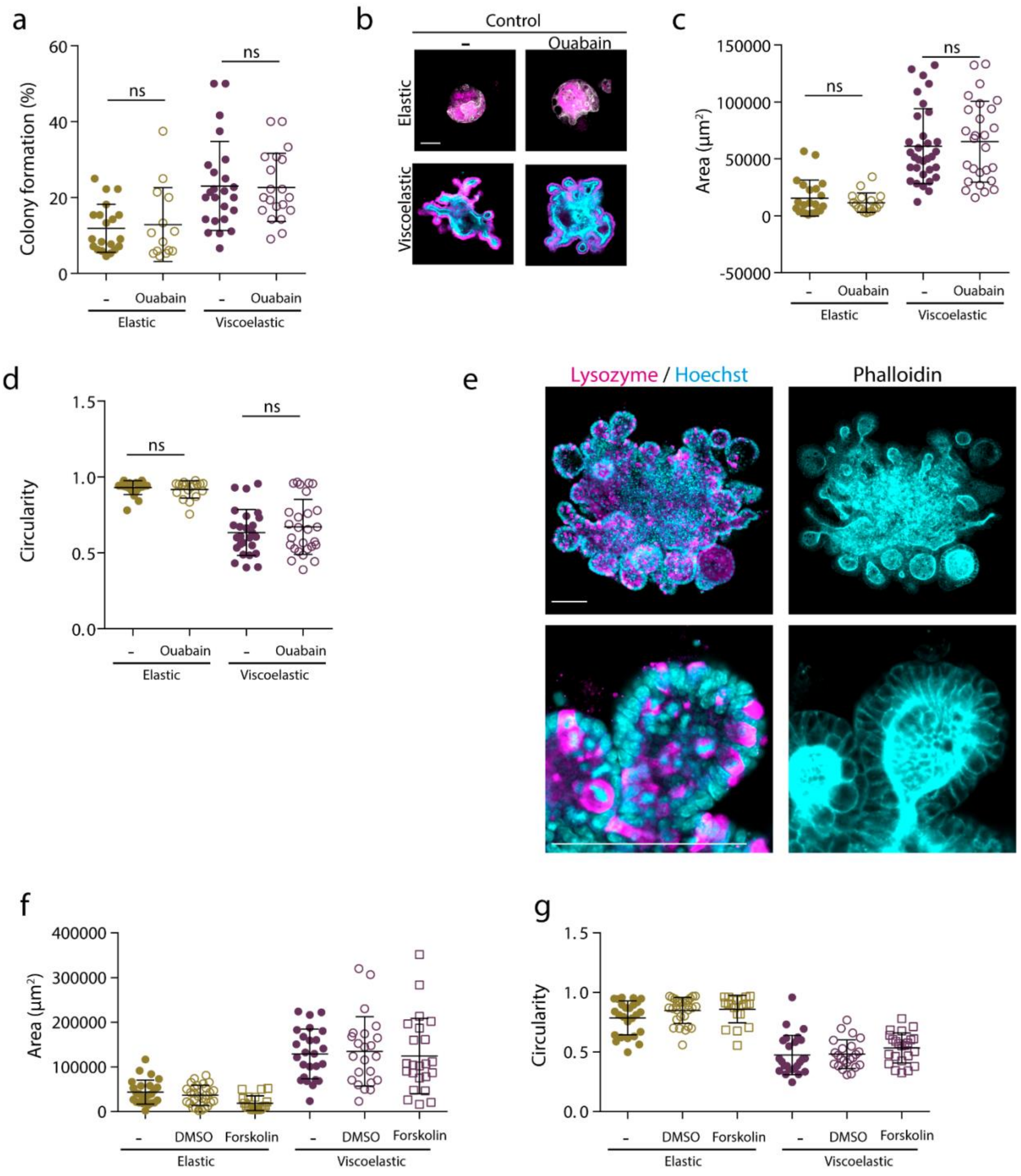

Supplementary Figure 14. Organoids grow, develop and pattern similarly in the presence of ouabain. a, Quantification of the percentage of cells which form colonies in gels after 7 days with or without ouabain. **b-d**, Representative examples (**b**) and quantification of organoids area (**c**) and circularity (**d**) after 7 days with or without ouabain in the culture medium. n=22,17,32,27 **b,c** / 20,14,24,20 **d** organoids per condition. Statistical analysis was performed using Kruskal–Wallis test followed by post hoc Dunn's test. **e**, Representative examples of Lysozyme, Hoechst and phalloidin stainings of organoids with ouabain.

Lysozyme (magenta) and Hoechst (cyan) in the left and phalloidin (cyan) in the right. Higher magnification images are provided on bottom row. **e-f**, Quantification of organoids area (**e**) and circularity (**f**) after 7 days with or without forskolin in the culture medium. n=25,28,20,25,23,20 organoids per condition. Statistical analysis was performed using Kruskal–Wallis test followed by post hoc Dunn's test. All data represent mean ± s.d., all scale bars are 100 µm.

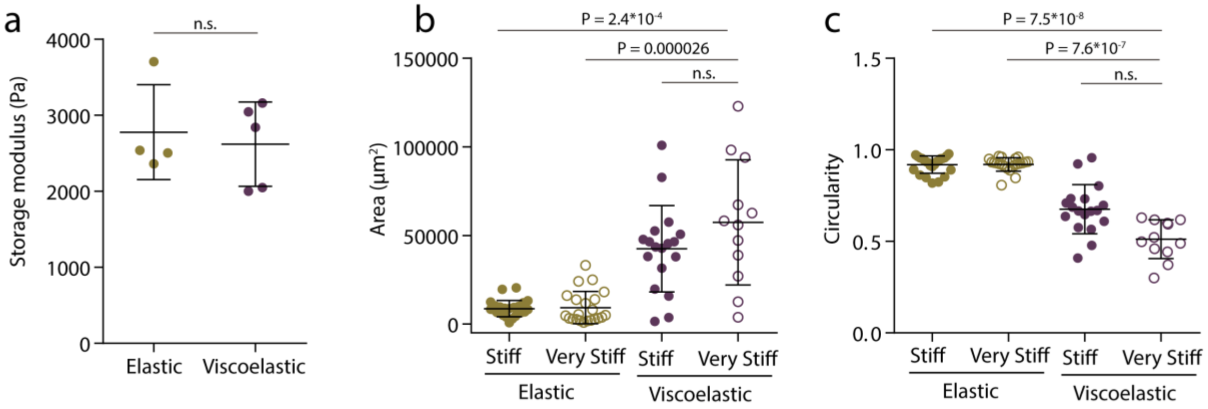

Supplementary Figure 15. Organoids morphological instability increases with stiffness in alginate-matrigel interpenetrating networks (IPN). a, Storage moduli of the elastic and viscoelastic alginate-matrigel IPNs. n=4,5 hydrogels per condition. Statistical analysis was performed using two-sided Mann-Whitney U-test. **b-c**, Quantification of the area (b) and circularity (c) of organoids in different stiffness elastic and viscoelastic matrices. b-c, n=24,22,18,12. Statistical analysis was performed using Kruskal–Wallis test followed by post hoc Dunn's test. All data represent mean ± s.d.

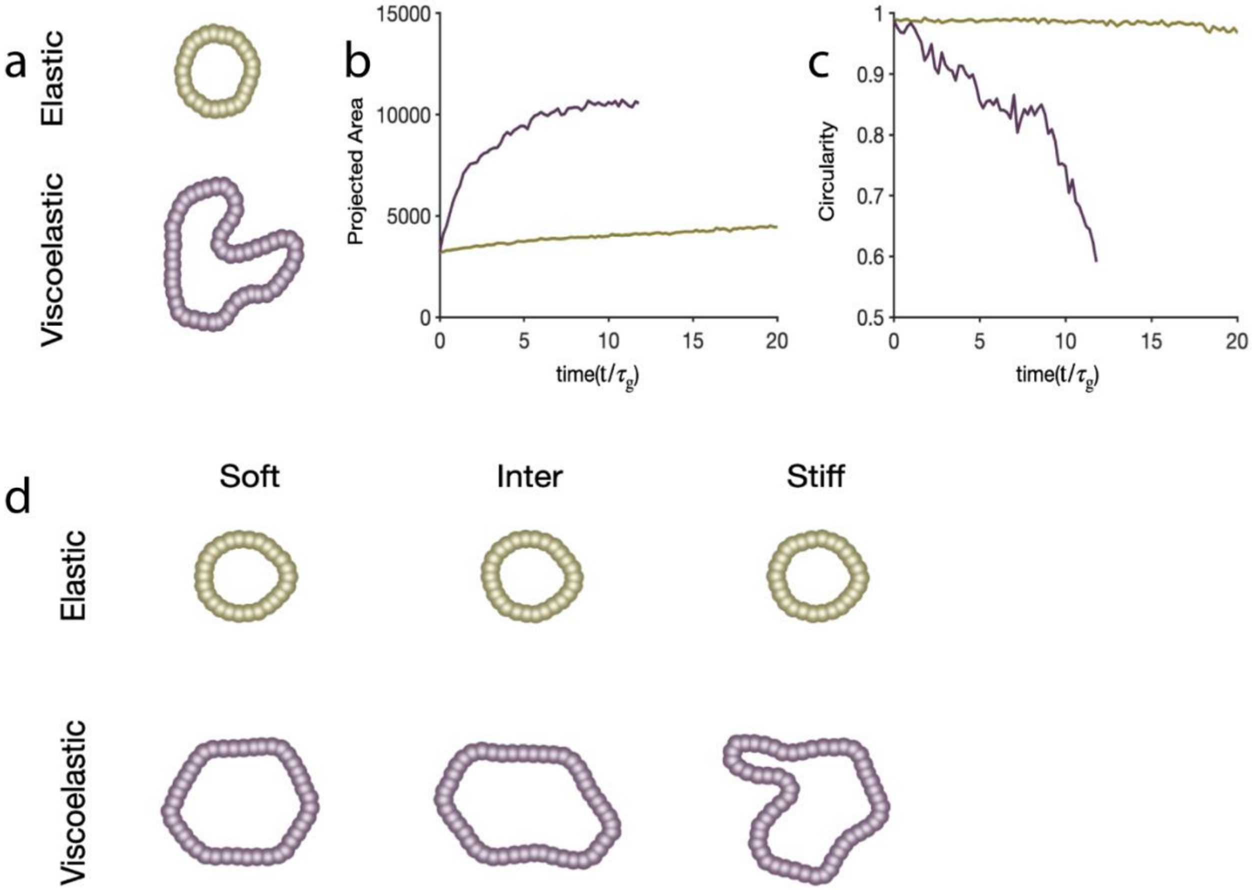

Supplementary Figure 16. Model Prediction: Organoids grow, break symmetry and form buds in viscoelastic matrices. a, Images of simulated organoids at time $(t = 12\tau_{\mathrm{g}})$ in stiff elastic and viscoelastic matrices. **b-c**, Simulation prediction of projected area (**b**) and circularity (**c**) evolution over time of organoids for the six matrix conditions. d, Images of simulated organoids at time $(t = 12\tau_{\mathrm{g}})$ with increasing stiffness in elastic matrices (top row) versus viscoelastic matrices (bottom row)

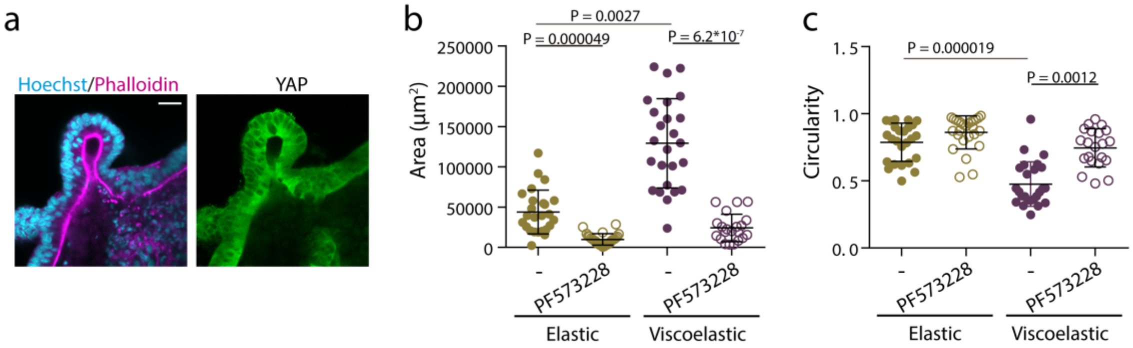

Supplementary Figure 17. Influence of YAP nuclear translocation and FAK in organoids development. **a**, Representative examples of phalloidin, Hoechst (left) and YAP (right) stainings of organoids in viscoelastic gels. **b-c**, Quantification of area (b) and circularity (c) in organoids in elastic and viscoelastic hydrogels without or with PF573228 (FAK inhibitor). n=25,26,25,21 organoids per condition. Statistical analysis was performed using Kruskal–Wallis test followed by post hoc Dunn's test. Scale bar is 20 µm. All data represent mean ± s.d.

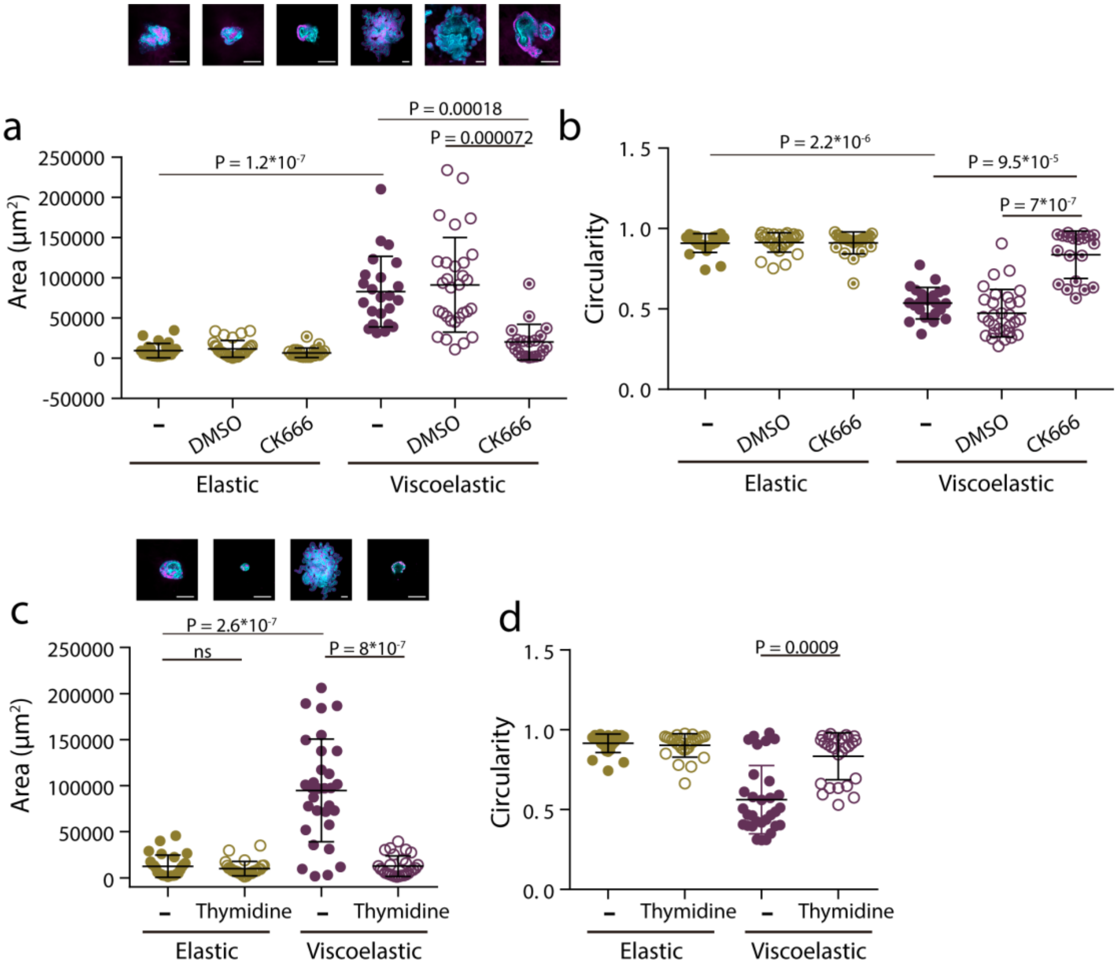

Supplementary Figure 18. Arp2/3 and cell proliferation regulate organoid growth and symmetry breaking. a-b, Representative examples and quantification of organoids (a) area and (b) circularity after 7 days in elastic and viscoelastic matrices with Arp2/3 (CK666) inhibitor. n= 23,28,23,23,30,20 organoids per condition. **c-d**, Representative examples and quantification of organoids (c) area and (d) circularity in elastic and viscoelastic matrices with thymidine. n=27,26,31,27 organoids per condition. Statistical analysis was performed using Kruskal–Wallis test followed by post hoc Dunn's test. Scale bars are 100 µm. All data represent mean ± s.d.

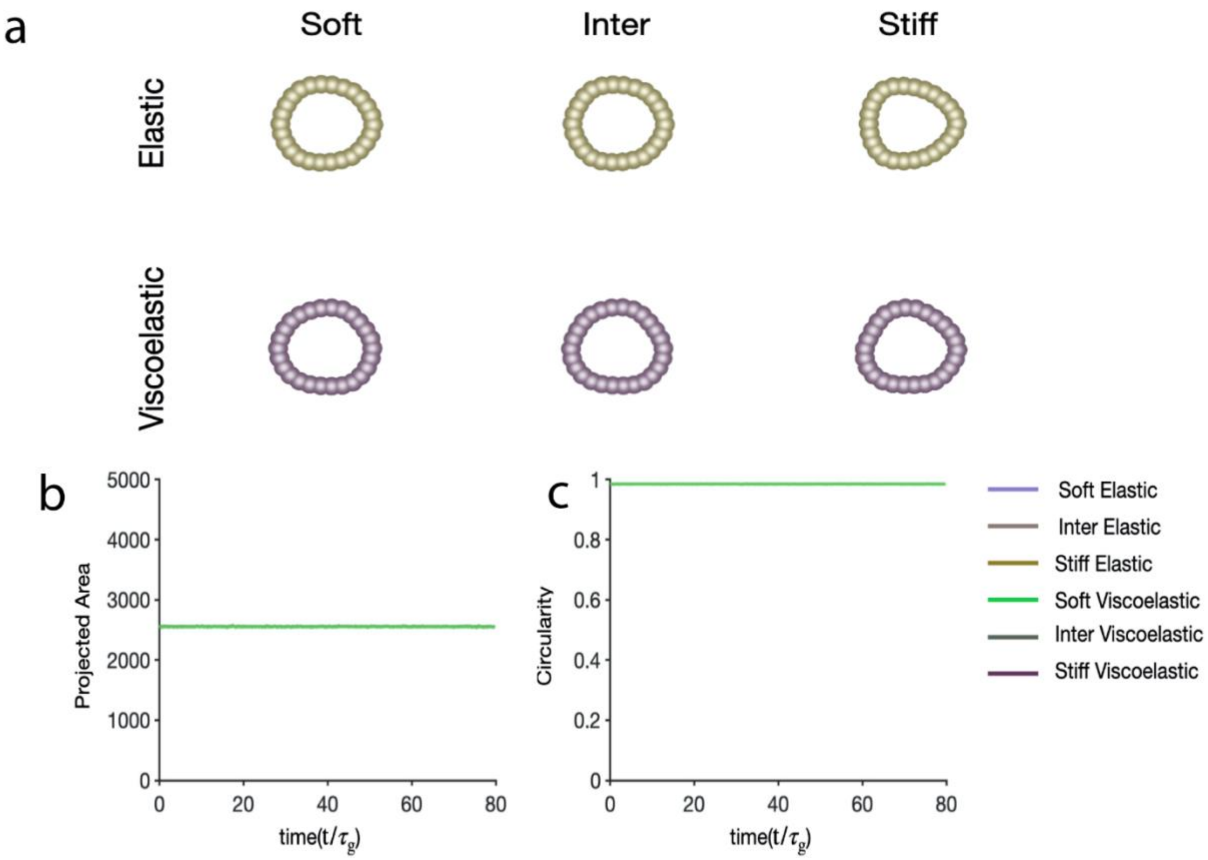

Supplementary Figure 19. Inhibition of cell motility prevents morphological instability, independently of the matrix viscoelasticity and stiffness. a, Images of simulated organoids at time $\left(t = 80\tau_{\mathrm{g}}\right)$ with increasing stiffness in elastic matrices (top row) versus viscoelastic matrices (bottom row) **b-c**, Simulation prediction of projected area (**b**) and circularity (**c**) evolution over time of organoids for the six matrix conditions.

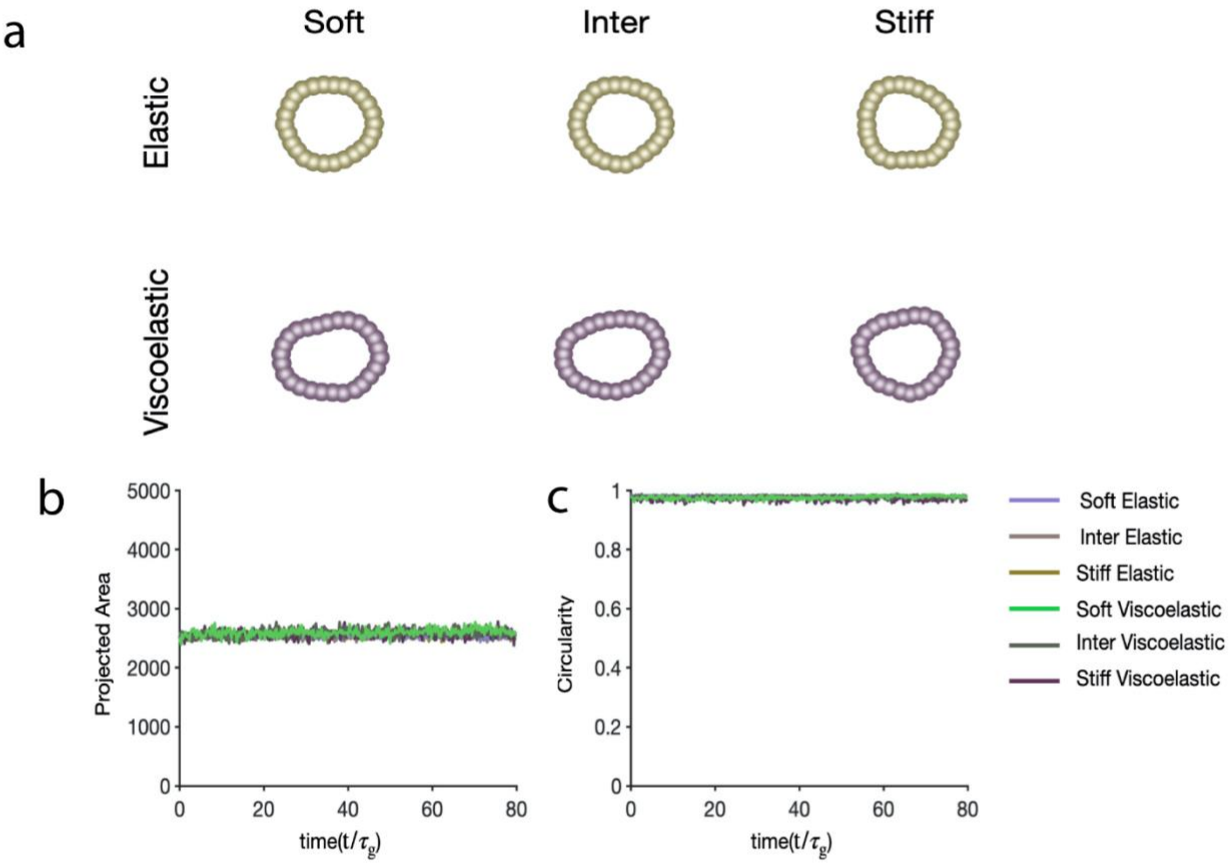

Supplementary Figure 20. Inhibition of cell proliferation prevents morphological instability independently of the matrix viscoelasticity and stiffness. a, Images of simulated organoids at time $(t = 80\tau_g)$ with increasing stiffness in elastic matrices (top row) versus viscoelastic matrices (bottom row) **b-c**, Simulation prediction of projected area (**b**) and circularity (**c**) evolution over time of organoids for the six matrix conditions.

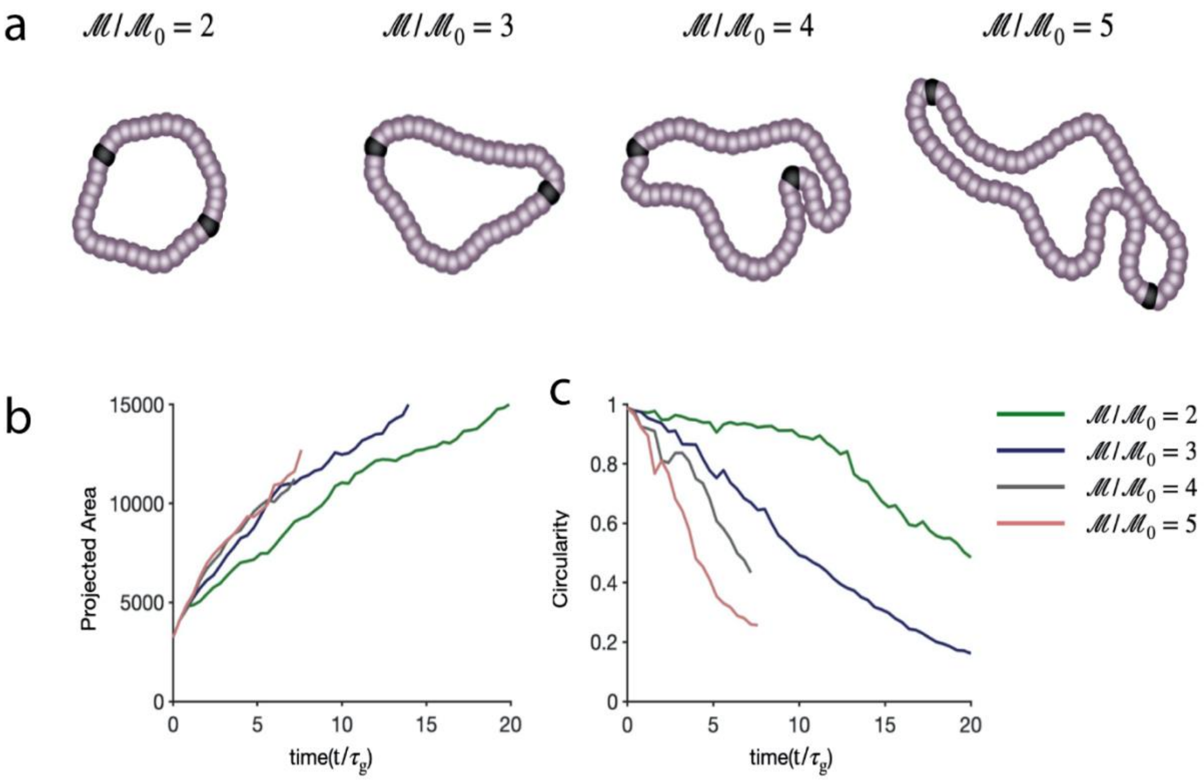

Supplementary Figure 21. Differential motility of cells in organoids affects the growth, symmetry breaking and budding of organoid. Black Cells have higher motility compare to the rest of the cells in the organoid **a,** Images of simulated organoids at time $(t \sim 8\tau_g)$ from left to right with increasing motility of the black cells in soft viscoelastic matrices **b-c**, Simulation prediction of projected area (**b**) and circularity (**c**) evolution over time of organoids with increasing motility of the black cells.

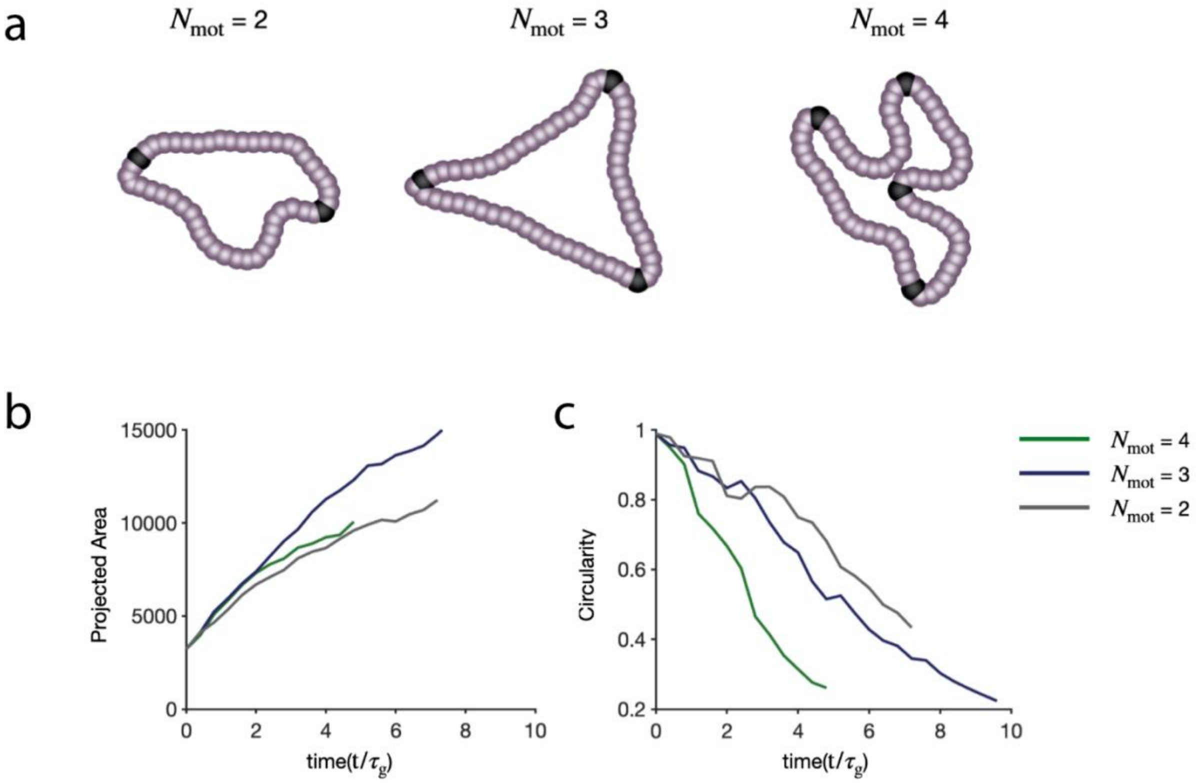

Supplementary Figure 22. Location of cell with differential motility is correlated with the location of symmetry breaking. a, Images of simulated organoids at time $\left(t\sim5\tau_{\mathrm{g}}\right)$ from left to right with increasing number of differentiated cells with relatively higher motility (shown in black) in soft viscoelastic matrices. **b-c**, Simulation prediction of projected area (**b**) and circularity (**c**) evolution over time of organoids with increasing number of differentiated cells with relatively higher motility.

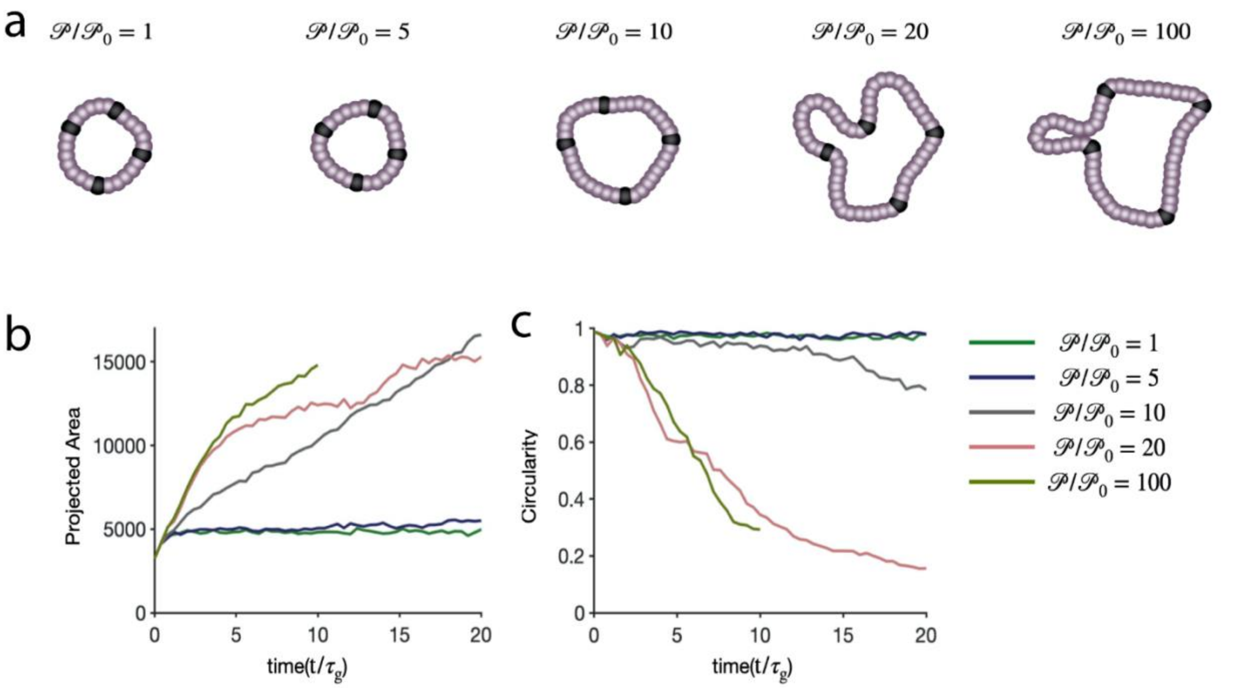

Supplementary Figure 23. Differential proliferation of cells in organoids affects the growth, symmetry breaking and budding of organoid. a, Images of simulated organoids at time $(t{\sim}10\tau_g)$ from left to right with increasing degree proliferation of differentiated cells (shown in black) in soft viscoelastic matrices **b-c**, Simulation prediction of projected area (**b**) and circularity (**c**) evolution over time of organoids with increasing proliferation of differentiated cells.

Supplementary Video S1: Examples of spheroids growth in elastic (left) and viscoelastic (right) matrices.

Supplementary Video S2: Examples of simulated tissue growth in elastic (left) and viscoelastic (right) matrices.

Supplementary Video S3: Examples of simulated tissue growth when cell motility is inhibited in elastic (left) and viscoelastic(right) matrices.

Supplementary Video S4: Examples of simulated tissue growth when cell proliferation is inhibited in elastic (left) and viscoelastic(right) matrices.

Supplementary Video S5: Examples of simulated tissue growth in elastic (upper row) and viscoelastic (lower row) in matrices of increasing stiffness.

Supplementary Video S6: Examples of simulated tissue growth when cell migration is inhibited in elastic (upper row) and viscoelastic (lower row) in matrices of increasing stiffness.

Supplementary Video S7: Examples of simulated tissue growth when cell proliferation is inhibited in elastic (upper row) and viscoelastic (lower row) in matrices of increasing stiffness.

Supplementary Video S8: Example of simulated tissue growth when cells are continuously added to the tissue in elastic (left) and viscoelastic (right) matrices.

Supplementary Video S9: Example of simulated tissue growth when the matrix property changes from elastic to viscoelastic.

Supplementary Video S10: Example of simulated tissue growth when the matrix property changes from viscoelastic to elastic.

Supplementary Video S11: Examples of simulated organoid tissue growth in elastic (upper row) and viscoelastic (lower row) in matrices of increasing stiffness.

Supplementary Video S12: Examples of simulated organoid tissue growth in viscoelastic matrices where two black cells have higher motility ($\mathcal{M}$) compared to the rest ($\mathcal{M}_0$).

Supplementary Video S13: Examples of simulated organoid tissue growth in viscoelastic matrices where an increasing number of cells (black) have 4 times higher motility compared to the rest.

Supplementary Video S14: Examples of simulated organoid tissue growth in viscoelastic matrices where four black cells have an increasing probability ($\mathcal{P}$) to divide compared to the rest ($\mathcal{P}_0$).

Theoretical model

In our experiments, a tissue comprised of motile, proliferating cells is initially encapsulated in a viscoelastic gel. Both the passive matrix and active cells are modeled using interacting soft spherical particles of size a subject to forces with appropriate Langevin dynamics. Initially, a collection of motile proliferating cells is surrounded by a passive set of particles representing the extracellular matrix. Cells are assumed to be active with a random movement analogous to a Brownian particle, but this movement is not related to temperature of the environment and is instead due to the active nature of the cell[1,2]. The cells also repel each other with a short-range force and also repel the matrix to avoid the overlap. The equation of motion for a cell with coordinate $\boldsymbol{r}_i^t$ is:

$$\mu_{\mathrm{t}}\,\dot{\boldsymbol{r}}_i^{\mathrm{t}} = -\frac{\partial U^{\mathrm{t}}}{\partial \boldsymbol{r}_i^{\mathrm{t}}} + \boldsymbol{\xi}_i(t)$$

where μ_t is the tissue viscous friction, U^{t} is the interaction potential for the cells, and $\boldsymbol{\xi}(t)$ is random force with zero mean and a variance related to its activity, i.e. $<\xi(t)>=0$; $<\xi_{i,\alpha}(t)\xi_{i,\beta}(t')>= 2\,\mathcal{M}\mu_{\mathrm{t}}\delta(t-t')\delta_{\alpha\beta}$. The viscous friction is a result of the interaction of cells with the extra-cellular matrix (ECM). Assumed that the inertial effects are negligible and hence considered an overdamped motion. The interaction potential for the cells, U^t has two contributions:

$$U^{\mathrm{t}}(\boldsymbol{x}) = \frac{1}{2}\Sigma_j\Sigma_{i\neq j}u_{ij}^{\mathrm{t}} + \frac{1}{2}\Sigma_k\Sigma_i u_{ik}^{\mathrm{tm}},$$

the first one is the interaction between the cells themselves, which we consider having short-range repulsion to avoid the overlap and mid-range (two cell size) attraction, and no long-range (greater than two cell size) interaction[3] :

$$u_{ij}^{\mathrm{t}} = \begin{cases} \epsilon\left(\left(\frac{a}{r_{ij}}\right)^2 - 1\right)\left(\left(\frac{r_c}{r_{ij}}\right)^2 - 1\right)^2 & \text{for } r_{ij} \le r_c \\ 0 & \text{for } r_{ij} > r_c \end{cases},$$

where $r_c = 2a$; the second one we assume that there is repulsive interaction between the cell and matrix of diameter `a' to avoid the overlap and that to be harmonic:

$$u_{ik}^{\mathrm{tm}} = \begin{cases} k_{\mathrm{tm}}\,(r_{ik} - a)^2 & \text{for } r_{ik} < a \\ 0 & \text{for } r_{ik} \geq a \end{cases},$$

where $r_{ij} = |\boldsymbol{r}_j^{\mathrm{t}} - \boldsymbol{r}_i^{\mathrm{t}}|$ is the distance between the cell 'i' and 'j' and $r_{ik} = |\boldsymbol{r}_k^{\mathrm{m}} - \boldsymbol{r}_i^{\mathrm{t}}|$ is the distance between the cell 'i' and matrix bead 'k'. The random force $\xi_i(t)$ is assumed to be zero-mean and uniformly distributed so that:

$$< \xi_{i,\alpha}(t) > = 0,$$

$$< \xi_{i,\alpha}(t)\xi_{i,\beta}(t') > = 2\,\mathcal{M}\mu_{\mathrm{t}}\delta(t - t')\delta_{\alpha\beta},$$

where is the single cell activity/motility and $\xi_{i,\alpha}$ is the x or y or z component of $\boldsymbol{\xi}_i$. By using the result from statistical physics[4], we can relate the microscopic diffusivity of a (Brownian) cell to the activity by the relation $D = \frac{\mathcal{M}}{\mu_{\mathrm{t}}}$.

In the model, the cell division has two constraints, a cell can divide only if it is older than a free growth-rate time scale τ_{g}, and a cell-division will be acceptable only if it is energetically favorable[5,6]. To decide the energetically favorable divisions, we are using a Metropolis-Hastings algorithm, a Markov chain Monte Carlo method[7]. At each time step we randomly pick a cell and check for the age of the cell, if the cell is older than τ_{g}, it is allowed to divide, the new cell will take space next to the old cell, with an angle which is chosen from a uniform random distribution over $[0 - 2\pi]$. We calculate the cost of energy $\Delta E = E_{\mathrm{f}} - E_{\mathrm{o}}$ to displace the cell and matrix, where $E_{\mathrm{f/o}}$ is the total energy of the cell aggregate and matrix after/before cell division. Then we accept this cell division with the probability:

$$P = \begin{cases} \exp\left(-\frac{\Delta E}{\mathcal{M}}\right) & \text{for } \Delta E \geq 0 \\ 1 & \text{for } \Delta E < 0 \end{cases}. \tag{1}$$

To model the matrix phase, we assume that the matrix is made of mono-disperse spherical bead of the same size as the cell 'a'. These beads are passive in nature and they get displaced as a reaction to tissue activity and pressure applied by the tissue proliferation. The bead moves under the influence of three forces: (i) the first arises from the elastic nature of the matrix with elasticity coefficient G'; the second arises from the interaction between the beads themselves, similar to what we have for the cell-cell interaction; and the last arises from the repulsion between the bead and the tissue to avoid the overlap. The equation of motion for a bead with coordinate $\boldsymbol{r}_i^{\mathrm{m}}$ is:

$$\mu_{\mathrm{m}} \ \dot{\boldsymbol{r}}_i^{\mathrm{m}} \ = -\frac{\partial U^{\mathrm{m}}}{\partial \boldsymbol{r}_i^{\mathrm{m}}}$$

where μ_m is the matrix viscous friction, U^m is the interaction potential for the matrix. Similar to the cell dynamics, we have assumed that the inertial effects are negligible and hence considered an overdamped motion. The interaction potential for the matrix U^{m} has three contributions:

$$U^{\mathrm{m}}(\boldsymbol{x}) = \frac{1}{2}\Sigma_i u_i^{\mathrm{E}} + \frac{1}{2}\Sigma_j \Sigma_{i \neq j} u_{ij}^{\mathrm{m}} + \frac{1}{2}\Sigma_k \Sigma_i u_{ik}^{\mathrm{tm}},$$

the first term is the elastic interaction for individual beads, we consider that each bead 'i' is attached to its initial position $\boldsymbol{r}_i^{\mathrm{m}-0}$ and if the bead gets displaced from its initial position to a new position $\boldsymbol{r}_i^{\mathrm{m}}$, due to the elastic nature bead tries to go back to its initial position. We assume the interaction to be:

$$u_i^{\mathrm{E}} = G'\left(\boldsymbol{r}_i^{\mathrm{m}} - \boldsymbol{r}_i^{\mathrm{m}-0}\right)^2;$$

where G' is the elasticity coefficient. If the distance of the bead to its attached position $\left|\boldsymbol{r}_i^{\mathrm{m}} - \boldsymbol{r}_i^{\mathrm{m}-0}\right| > 0.5a$, we assume that the bead breaks away from its attached position and acquires a new attached position which is its current position, i.e., $\boldsymbol{r}_i^{\mathrm{m}-0} = \boldsymbol{r}_i^{\mathrm{m}}$. The second term is the interaction between the beads themselves, which we consider having short-range repulsion to avoid the overlap and mid-range (two bead size) attraction, and no long-range (greater than two bead size) interaction[7]:

$$u_{ij}^{\mathrm{m}} = \begin{cases} \epsilon\left(\left(\frac{a}{r_{ij}}\right)^2 - 1\right)\left(\left(\frac{r_c}{r_{ij}}\right)^2 - 1\right)^2 & \text{for } r_{ij} \leq r_c \\ 0 & \text{for } r_{ij} > r_c \end{cases};$$

where $r_c = 2a$; the third term is due to the repulsive interaction between the bead and the cell of diameter \`a' to avoid the overlap and that to be harmonic:

$$u_{ik}^{\mathrm{tm}} = \begin{cases} k_{\mathrm{tm}}\,(r_{ik} - a)^2 & \text{for } r_{ik} < a \\ 0 & \text{for } r_{ik} \geq a \end{cases},$$

where $r_{ij} = |\boldsymbol{r}_j^{\mathrm{m}} - \boldsymbol{r}_i^{\mathrm{m}}|$ is the distance between the bead 'i' and 'j' and $r_{ik} = |\boldsymbol{r}_k^{\mathrm{t}} - \boldsymbol{r}_i^{\mathrm{m}}|$ is the distance between the cell 'k' and matrix bead 'i'.

Initial Setup

We start with a spherical ball of cells of radius $R_0 = 4a$, which is made of 79 cells (except mentioned otherwise) and these cells are uniformly, randomly distributed within the spherical ball. This spherical ball of cells is surrounded by a concentric spherical shell of matrix of inner radius $R_{in} = 5a$ and outer radius $R_{out} = 12a$, which is made of 6330 beads (except mentioned otherwise) and these beads are tightly packed in an orderly fashion on the surface of a sphere with radius $'ka'(k \in [R_{in} - R_{out}])$ within the spherical shell. We keep the tissue viscosity μ_{t} fixed for all the simulations except at the very end. We vary the matrix viscosity such that the viscosity ration $\mu = \frac{\mu_{\mathrm{t}}}{\mu_{\mathrm{m}}} = 0.002 \text{ and } 2$ for the viscoelastic and the elastic case, respectively. To change the stiffness, we vary the matrix elasticity coefficient $G' = 05, 50, \& \ 100$ for the soft, intermediate, and stiff case, respectively, varying the matrix relaxation time $\tau_{\mathrm{m}} = \frac{\mu_{\mathrm{m}}}{G'}$. To accommodate the linear relationship between the stiffness and the random motility of the cells, we use a linear relationship between stiffness and motility, and for three different stiffness of the matrix, we use the cell motility parameter $M = 0.2, 0.8, \& \ 1.6$ for the soft, intermediate, and stiff matrix case, respectively. For the intermediate viscoelastic matrix, *i.e.*, $\mu_m = 10, G' = 50$, and the stiff viscoelastic case, i.e., $\mu_m = 10, G' = 100$, the proliferation is high and long fingers of the tissue exceed the matrix environment, to prevent this we used a thicker matrix with outer radius of the spherical shell $R_{out} = 14 \ \& \ 20$, respectively. We used 10,240 & 30,710 beads in the matrix for the intermediate and stiff viscoelastic cases, respectively. For the stiff viscoelastic matrix case the proliferation is significantly high (Fig. 3c,j) and even with this thick matrix of size $R_{out} = 20$, with 30,710 beads, we could capture the correct physics only up to time $\sim 180 \ \tau_g$, and the simulations after this time show that the fingers of tissues started to outgrow the matrix size. We did more than one simulation for all the six matrix cases mentioned above, *i.e.*, soft elastic & viscoelastic; intermediate elastic & viscoelastic; stiff elastic & viscoelastic; and they show statistically similar behavior.

For the case where we inhibit the cell motility, we use a very small motility parameter $M = 0.01$, for all the six conditions. For the case, where we inhibit the cell proliferation, we have used a slightly higher number of cells, i.e., 113, to start with a densely packed the spherical ball of the cells, as the number of cells will not increase with time. We performed two sets of simulation with the six conditions of matrix, for the cases where motility has been inhibited and where proliferation has been inhibited.

Simulations for phase diagram

To explore the regimes of morphological stability, in terms of the three dimensionless parameters, we change the tissue viscosity ratio $\mu = \frac{\mu_t}{\mu_m}$ from $0.001 - 2$. For each case of tissue viscosity ratio μ, we consider three cases of stiffness, i.e., $G' = 5, 50, \& \ 100$, and perform the simulations. Since, the cell proliferation is an indirect function matrix rheology, the scaled cell flux $j = \frac{\tau_g}{\tau_t}$ is an emergent parameter, recalling τ_t is the time it takes to add one cell to the tissue. We observe both in experiments and simulations that as we decrease the matrix viscosity μ_m and increase the matrix stiffness G', cell proliferation increases and hence cell flux j increases. In our experiments the highest cell proliferation occurs in the Stiff Viscoelastic matrix and using linear regression we estimate that the tissue doubles in size in 20.5hr. This corresponds to value of $\tau_t \sim 37s$ in the stiff viscoelastic matrices; in contrast, $\tau_t \sim 330$s in stiff elastic matrices due to its much slower tissue growth. These are in the same order of magnitude of the relaxation times of the matrices. The resulting cell flux, when the initial spheroid is composed of 2000 cells, is $j = 0.027$. For the stiff elastic case, $j = 0.0030$.

To generate the phase-diagram we developed a custom Matlab software and used support vector machines (SVM) classifier for binary classification. For the cases where motility is small, thence the proliferation is small, i.e., $j \sim 0$, the growth of the spheroidal tissue for all the conditions were stable. We have plotted the corresponding two-dimensional phase-diagram (Extended Data Fig.8b) and the background looks completely blue, an indicator that the tissue growth for the scaled cell flux $j \sim 0$ is always stable. The data from actual simulations were represented as blue dots. For moderate values of scaled cell flux $j \sim O(1)$, we have plotted a three-dimensional phase diagram (Fig 5, Extended Data Fig.8a). We observe that as the scaled proliferation increases the region of stability starts to shrink in $\mu - A$ plane and eventually the whole phase space becomes unstable.

Controlled cell flux driven simulations

For the controlled cell flux driven tissue growth, we relax the stress dependent cell proliferation condition. With this relaxed constraint, we add one cell (mass) after time τ_t at the center of the tissue to mimic the experiments, where the cell flux injection is controlled, and new cells (mass) are being added at the center of the tissue. By controlling τ_t we can control the cell flux injection rate, which gives us a precise control over scaled cell flux j. This was not the case for stress dependent cell proliferation simulations. We vary the proliferation time scale $\tau_t \in [0.1 - 1]$ to control the scaled cell flux j.

Using the data from our simulations we have generated a two-dimensional Phase-diagram (Extended Data Fig.8c) for the controlled flux driven case. We have fixed the scaled cell flux $j = 10$, and varied the viscosity ratio $\mu \in [0.1 - 10]$ for the three values of elasticity $G' = 0$ (to mimic the viscous Saffman-Taylor instability[8]), 0.1 (softer than the control soft matrix case) , and 5 (soft matrix). The phase-diagram (Extended Data Fig.8c) shows an opposite trend where the region close to origin (elastic matrices, Extended Data Fig. 7d,e) becomes unstable and the region away from origin (viscoelastic matrices, Extended Data Fig. 7d,e) becomes stable. The data from actual simulations were represented as blue dots for spheroidal growth of the tissue and red dots for the branched growth of the tissue.

Simulations with dynamic change in viscosity of the matrix

To see the effects of dynamic change in the viscosity of the matrix on the tissue growth, we considered two cases: (i) At the start of the simulation, matrix is elastic $\left(A = \frac{\tau_\mathrm{a}}{\tau_\mathrm{m}} = 0.017, \mu = \frac{\mu_\mathrm{t}}{\mu_\mathrm{m}} = 0.002, j = \frac{\tau_\mathrm{g}}{\tau_\mathrm{t}} = 0.05\right)$ in nature and after a certain time ($15\ \tau_\mathrm{g}$) matrix smoothly changes its viscous property and becomes viscoelastic $\left(A = \frac{\tau_\mathrm{a}}{\tau_\mathrm{m}} = 133, \mu = \frac{\mu_\mathrm{t}}{\mu_\mathrm{m}} = 2, j = \frac{\tau_\mathrm{g}}{\tau_\mathrm{t}} = 0.16\right)$ in nature (ii) At the start of the simulation, the matrix is viscoelastic $\left(A = \frac{\tau_\mathrm{a}}{\tau_\mathrm{m}} = 133, \mu = \frac{\mu_\mathrm{t}}{\mu_\mathrm{m}} = 2, j = \frac{\tau_\mathrm{g}}{\tau_\mathrm{t}} = 0.16\right)$ in nature and after certain time ($15\ \tau_\mathrm{g}$) matrix smoothly changes its viscous property and becomes elastic $\left(A = \frac{\tau_\mathrm{a}}{\tau_\mathrm{m}} = 0.017, \mu = \frac{\mu_\mathrm{t}}{\mu_\mathrm{m}} = 0.002, j = \frac{\tau_\mathrm{g}}{\tau_\mathrm{t}} = 0.05\right)$ (Supplementary Fig 5 a). In both the cases matrix maintains it stiffness (G') and it changes only its viscosity μ_m to control the viscoelasticity of the matrix. The property of the tissue is same for both of these cases. In Supplementary Fig. 5 b, we show the images of the evolution of the tissue for case (i) (top row) and case (ii) (bottom row). For case (i) we see that as soon as we start to reduce the viscosity, there is rapid growth of spheroidal tissue, the spheroid starts to break the symmetry and eventually budding starts. The same can be confirmed from the Supplementary Fig. 5 c-d, where we have quantified the area and circularity of the cross-section of the tissue. There is sudden increase in the area and reduction in the circularity as we change the property of the matrix from elastic to viscoelastic. For case (ii) we see that initially, the growth of the spheroidal tissue is rapid, there are initial signs of budding, but as we increase the viscosity of the matrix, there is arrest of growth and there is no new bud formation. We further quantified it by looking at the area and circularity of the cross-section of the spheroidal tissue. As soon as the viscosity of the matrix increases there is arrest in the growth of the cross-sectional area of the tissue and rapid decrease in the circularity stops, reverses the trend with slow increase in the overall circularity value with time. These results indicate that by dynamically changing the property of the ECM (decreasing the viscosity of the matrix) around the tissue we can go from morphologically stable to morphologically unstable tissue growth (case i) and similarly by increasing the viscosity of the ECM we can control the morphologically unstable tissue growth (case ii).

Simulations of the Organoids

In our experiments, an organoid comprised of motile, proliferating epithelial cells is initially encapsulated in a viscoelastic gel. The model for spheroidal tissue growth is modified to simulate the organoid by changing the cell-cell interaction. We perform the simulations for a two-dimensional organoid model. In the model, the organoid cells are arranged as a chain of cells to mimic the cross-section of an organoid. These cells are always linked to their neighbors through a spring (to avoid stretching and compression) and try to maintain an angle of π between two neighboring connections (to avoid bending). In a relaxed state, this interaction puts the cells of the organoid on the circumference of a perfect circle. The inter-cellular interaction for the organoid will have two contributions, one from the stretching/compression and the other from the bending. The interaction potential for a cell will be given by

$$u_i^{\mathrm{t}} = \frac{1}{2} k_s [(\boldsymbol{r}_i - \boldsymbol{r}_{i-1} - a)^2 + (\boldsymbol{r}_i - \boldsymbol{r}_{i-1} - a)^2] + \frac{1}{2} k_b (\widehat{\boldsymbol{n}_{-1}} - \widehat{\boldsymbol{n}_1})^2,$$

Where k_s is spring coefficient and k_b is bending coefficient, $\widehat{\boldsymbol{n}_{-1}}$ and $\widehat{\boldsymbol{n}_1}$ are the unit vector in the direction $(\boldsymbol{r}_i - \boldsymbol{r}_{i-1})$ and $(\boldsymbol{r}_i - \boldsymbol{r}_{i+1)}$, respectively. $'i-1'$ and $'i+1'$ are the left and right neighbors of the cell $'i'$, respectively. There is periodicity for the chain of cells, which means for cell number $i = 1$, the $i - 1 = N$, and for cell number $i = 1$, the $i + 1 = 1$. N is total number of cells in the organoid at a given instant.

The total interaction potential U^t for the system of cells will have two contributions similar to spheroidal model:

$$U^{\mathrm{t}}(\boldsymbol{x}) = \frac{1}{2}\Sigma_i u_i^{\mathrm{t}} + \frac{1}{2}\Sigma_k \Sigma_i u_{ik}^{\mathrm{tm}},$$

Where u_i^t is the contribution from the cell-cell interaction which we have defined in the previous paragraph and u_{ik}^{tm} is the contribution from the tissue-matrix interaction, which we are keeping same as spheroidal-tissue model. The interaction potential for the matrix is same as the spheroidal-tissue model. The dynamics of the position of the cell and the bead of the matrix is same as the spheroidal-tissue model. In the organoid model, the cell division has the same criterion as in the spheroidal tissue model. If a new cell-division happens it takes a position between two cells with a probability which is local stress dependent.

Initial Setup for the Organoids

All the simulations for the organoid start with $N = 26$ cells, which are placed at the circumference of circle of radius $4a$. This circle of cells is surrounded by a concentric annulus of matrix of inner radius $R_{in} = 5a$ and outer radius $R_{out} = 14a$, which is made of 655 beads (except mentioned otherwise) and these beads are tightly packed in an orderly fashion on the periphery of a circle with radius $'ka'(k \in [R_{in} - R_{out}])$ within the annulus. We terminate the simulation once the organoid touches the outer radius of the matrix.

We have considered six matrix cases to see the effect of stiffness and the viscosity on the organoidal growth. We have considered the viscosity ratios $\frac{\mu_t}{\mu_m} = 0.002$ and $\frac{\mu_t}{\mu_m} = 2$, same as spheroidal model, and call them as elastic and viscoelastic matrix, respectively. For each case of viscosity ratio μ, we consider three cases of stiffness, i.e., $G' = 5, 50, \& \ 100$, call them soft, intermediate and stiff respectively, and perform the simulations.

In Supplementary Fig 16 a, we show the images of organoids for stiff elastic (top) and stiff viscoelastic case (bottom) at time $t = 12\tau_{\mathrm{g}}$. Supplementary Fig 16 b-c, show that for viscoelastic cases the organoids grow rapidly and break their circular symmetry and become morphologically unstable, whereas for elastic case the organoid growth remains stable and circularly symmetric. Supplementary Fig 16 d, show the images of organoids for elastic (top row) and viscoelastic case (bottom row) with increasing stiffness (left to right) at time $t = 12\tau_{\mathrm{g}}$. With increasing stiffness, the symmetry breaking is more prominent for viscoelastic case, whereas the effect of stiffness is milder for elastic case. The finding that the organoids are morphologically stable in elastic matrices and morphologically unstable in the viscoelastic matrices and with stiffness their growth increases, and circularity decreases is in good agreement with the experiments and similar to what we have found in our spheroidal tissue simulations.

In Supplementary Fig. 19, we have reduced the motility of the organoid cells $(\mathcal{M} \sim 0)$ and we find that independent of viscosity and stiffness the growth of the organoid is stalled (Supplementary Fig. 19b) and organoid maintains a circularly symmetrical morphology (Supplementary Fig. 19c).

In Supplementary Fig. 20, we have reduced the proliferative capacity to zero the organoid cells $(j \sim 0)$ and we find that independent of viscosity and stiffness the growth of the organoid is stalled (Supplementary Fig. 20b) and organoid maintains a circularly symmetrical morphology (Supplementary Data Fig. 20c).

Organoids with multiple cell types

To test whether the change in cell type within the organoid can be correlated with location of the symmetry breaking, we considered two simple cases where we placed cells at given locations in the organoid (i) with relatively higher motility compare to the rest of the cells of organoid (ii) with relatively higher proliferation rate compare to the rest of the cells of organoid. For all these tests, we considered the evolution of organoid in the soft-viscoelastic matrix.

Case i: Cells with High Motility

We first investigated the effect of intensity of relative motility $\left(\frac{\mathcal{M}}{\mathcal{M}_0}\right)$ and then for a fixed relative motility the effect of number of high motile cells N_{mot} on the growth of the organoid.

We replaced two of the normal cells in the organoid with highly motile cells. We increased the degree of motility systematically, e.g., motility ratio $\frac{\mathcal{M}}{\mathcal{M}_0} = 2,3,4 \;\&\; 5$, and looked at the growth of organoid. We find that the addition of highly motile cells enhances the morphological disorder (Supplementary Fig. 21). In the Supplementary Fig. 21a, we show the images of the organoid at time $t = 8\tau_{\mathrm{g}}$ with the increasing degree of motility ratio $\frac{\mathcal{M}}{\mathcal{M}_0}$. For $\frac{\mathcal{M}}{\mathcal{M}_0} = 2$, the location of the morphological instabilities are not correlated with the position of the cells with high motility but for the case $\frac{\mathcal{M}}{\mathcal{M}_0} = 3,4, \& \; 5$, the location of the morphological instability is directly correlated with the position of the high motility cells (black color cells in Supplementary Fig 21a). In Supplementary Fig 21b-c, we have reported the area and circularity of the organoid with increasing degree of motility, we find that growth of organoid is same for $\frac{\mathcal{M}}{\mathcal{M}_0} = 3,4, \& \; 5$ (Supplementary Fig 21b) but the circularity decreases (morphological instability increases) with increasing degree of motility (Supplementary Fig 21c). This implies that replacing a few regular organoid cells with highly motile cells will not affect the growth (the smaller motility of the rest of the cells will dominate the growth) but it will definitely affect the morphological instability of the organoid.

To ensure that the location of the cells with high motility is directly correlated with the location of the morphological instabilities, we increase the number of cells with high motility. We kept the motility ratio fixed to $\frac{\mathcal{M}}{\mathcal{M}_0} = 4$, and systematically increased the number of cells with high motility $N_{\mathrm{mot}} = 2,3, \& \ 4$. In Supplementary Fig 22 a, we show that the location of morphological instabilities are directly correlated with the highly motile cells (black color cells). In Supplementary Fig 22 b-c, we report the area and circularity of the organoid with increasing number of high motile cells N_{mot}, we see that there is an increase in growth and decrease in the circularity of the organoid with increasing N_{mot}.

Case ii: Cells with High Proliferation

To study the effect of the cells with relative high proliferation on the growth of the organoid, we replaced four of the normal cells in the organoid with cells of high proliferation. To control the proliferation in the model, we add an additional control on the probability with which we accept the cell division for $\Delta E > 0$ is $\exp\left(-\frac{\mathcal{P}_0}{\mathcal{P}}\frac{8\Delta E}{\mathcal{M}}\right)$, for regular cell $\mathcal{P} = \mathcal{P}_0$, which brings back the regular probability for the regular cells of the organoid to accept the cell division. Since, the growth of organoid is morphologically unstable in soft viscoelastic matrix (Supplementary Fig 16), so we have increased the energy cost for the cell division by a factor 8, i.e., $8\Delta E$ to reduce the proliferation of all the cells of the organoid in general, this gives us a morphologically stable organoid when all cells are of same kind $\left(\frac{\mathcal{P}}{\mathcal{P}_0} = 1\right)$. We are systematically increasing the degree of proliferation, i.e., $\frac{\mathcal{P}}{\mathcal{P}_0} = 1, 5, 10, 20 \ \& \ 100$. In Supplementary Fig 23 a, we show the images of the organoid at time $t \sim 10\tau_{\mathrm{g}}$, for $\frac{\mathcal{P}}{\mathcal{P}_0} = 1 \ \& \ 5$; the growth of the organoid is morphologically stable; only when the degree of proliferation crosses a certain value, e.g., $\left(\frac{\mathcal{P}}{\mathcal{P}_0} = 10,20 \ \&100\right)$, the organoid becomes morphologically unstable. We observe that when the organoids become morphologically unstable the location of the instabilities are directly correlated with the position of the cells with high proliferation (the two images in the right of Supplementary Fig 23 a). In Supplementary Fig 23 b-c, we reported the area and circularity of the organoid for the cells with high proliferation. The growth increases and circularity decreases (morphological instability increases) with the increase in the degree of proliferation of the cells with high proliferation.

Simulation Methods

We developed an inhouse Fortran-90 code to model the growth of spheroids in a viscoelastic matrix. The simulations were performed using the Euler-Maruyama method with a Langevin term and integrating in time. We use reduced, dimensionless unit, all lengths in terms of typical cell size 'a', $r^* = r/a$; and all the time in terms of cell proliferation time τ_g; $t^* = t/\tau_g$. We use Mersenne Twister algorithm, a pseudorandom number generator, to generate the random numbers.

Quantification of tissue shape properties of simulations

A custom MATLAB software was developed to measure, during the simulations, the tissue shape properties. Briefly, as the simulations are performed assuming that cells are discrete points, we first spherically dilate each point to generate a continuous volume. Then, once we have the connected mesh, the volume and sphericity are quantified. The area and circularity were quantified from the middle plane of the spheroid.

Supplementary Table 1. Alginate hydrogel composition.

Alginate Molecular weight (kDa)	Stiffness (Pa)	Alginate (%)	Calcium sulphate (mM)
138	390	2	16.8
138	1855	2	28.8

138	4959	2	57.6
38	409	2	33.6
38	1618	2	52.8
38	5095	2	96

Supplementary Table 2. Table for dimensionless quantities in the simulation.

Parameter	Simulations	Experiments
Cell Size (a)	$10^{-5}\mathrm{m}$	$\sim 10^{-5}\mathrm{m}$
Motility Speed $\left(\mathrm{v}_{\mathrm{mig}} = \frac{D}{a}\right)$	$1 \times 10^{-9} - 1 \times 10^{-6}$ m/s	~5 $\times 10^{-8}\mathrm{m/s}$
Activity Time Scale $\left(\tau_{\mathrm{a}} = \frac{M}{\epsilon}\tau_{\mathrm{g}}\right)$	7-54 s	~2-40s[9-11]
Viscoelastic Time Scale $\left(\tau_{\mathrm{m}} = \frac{G'}{\mu_{\mathrm{m}}}\right)$	0.5-1000 s	30-350 s
Viscosity Ratio $\left(\mu = \frac{\mu_{\mathrm{t}}}{\mu_{\mathrm{m}}}\right)$	0.001-2	0.00019-0.066
Scaled Activity $\left(A = \frac{\tau_{\mathrm{a}}}{\tau_{\mathrm{m}}}\right)$	0.1-100	0.028-40
Scaled Cell Flux $\left(j = \frac{\tau_{\mathrm{g}}}{\tau_{\mathrm{t}}}\right)$	0.002-10	~0.003-166

Supplementary Table 3. Alginate-matrigel interpenetrating networks composition.

Alginate Molecular weight (kDa)	Stiffness (Pa)	Alginate (%)	Matrigel (mg/ml)	Calcium sulfate (mM)
138	473	1	5	26.4
138	1489	1	5	48
38	452	1	5	48
38	1422	1	5	96

References:

1 Berthier, L. & Kurchan, J. Non-equilibrium glass transitions in driven and active matter. *Nature Physics* **9**, 310-314, doi:10.1038/nphys2592 (2013).

2 Mallory, S. A., Šarić, A., Valeriani, C. & Cacciuto, A. Anomalous thermomechanical properties of a self-propelled colloidal fluid. *Physical Review E* **89**, 052303, doi:10.1103/PhysRevE.89.052303 (2014).

3 Wang, X., Ramírez-Hinestrosa, S., Dobnikar, J. & Frenkel, D. The Lennard-Jones potential: when (not) to use it. *Physical Chemistry Chemical Physics* **22**, 10624-10633, doi:10.1039/C9CP05445F (2020).

4 Kardar, M. *Statistical Physics of Fields*. (Cambridge University Press, 2007).

5 Uroz, M. *et al.* Regulation of cell cycle progression by cell-cell and cell-matrix forces. *Nature cell biology* **20**, 646-654, doi:10.1038/s41556-018-0107-2 (2018).

6 Delarue, M. *et al.* Compressive Stress Inhibits Proliferation in Tumor Spheroids through a Volume Limitation. *Biophysical journal* **107**, 1821-1828, doi:https://doi.org/10.1016/j.bpj.2014.08.031 (2014).

7 Hastings, W. K. Monte Carlo Sampling Methods Using Markov Chains and Their Applications. *Biometrika* **57**, 97-109, doi:10.2307/2334940 (1970).

8 Saffman, P. G. & Taylor, G. I. The penetration of a fluid into a porous medium or Hele-Shaw cell containing a more viscous liquid. *Proceedings of the Royal Society of London. Series A. Mathematical and Physical Sciences* **245**, 312-329, doi:doi:10.1098/rspa.1958.0085 (1958).

9 Liu, Z. *et al.* Mechanical tugging force regulates the size of cell-cell junctions. *Proceedings of the National Academy of Sciences of the United States of America* **107**, 9944-9949, doi:10.1073/pnas.0914547107 (2010).

10 Maruthamuthu, V., Sabass, B., Schwarz, U. S. & Gardel, M. L. Cell-ECM traction force modulates endogenous tension at cell-cell contacts. *Proceedings of the National Academy of Sciences of the United States of America* **108**, 4708-4713, doi:10.1073/pnas.1011123108 (2011).

11 Maitre, J. L. & Heisenberg, C. P. The role of adhesion energy in controlling cell-cell contacts. *Current opinion in cell biology* **23**, 508-514, doi:10.1016/j.ceb.2011.07.004 (2011).